Alpha-case promotes fatigue cracks initiation from the surface in heat treated Ti-6Al-4V fabricated by Laser Powder Bed Fusion

Quentin Gaillard, Florian Steinhilber, Amélie Larguier, X Boulnat, Jean-Yves Buffiere, Guilhem Martin, Sylvain Dancette, Sophie Cazottes, Rémy Dendievel, Christophe Desrayaud

International Journal of Fatigue 190 (2025) 108621

Contents lists available at ScienceDirect

International Journal of Fatigue

journal homepage: www.elsevier.com/locate/ijfatigue

Alpha-case promotes fatigue cracks initiation from the surface in heat treated Ti-6Al-4V fabricated by Laser Powder Bed Fusion

Quentin Gaillard [a,b,*], Florian Steinhilber [b,c], Amélie Larguier [b], Xavier Boulnat [b], Jean-Yves Buffiere [b], Guilhem Martin [c], Sylvain Dancette [b,d], Sophie Cazottes [b], Rémy Dendievel [c], Christophe Desrayaud [a]

[a] Mines Saint-Etienne, Univ. Lyon, CNRS, UMR 5307 LGF, F-42023 Saint-Etienne, France
[b] Univ. Lyon, INSA Lyon, CNRS, UMR 5510 MATEIS, F-69621 Villeurbanne, France
[c] Univ. Grenoble Alpes, Grenoble INP, CNRS, UMR 5266 SIMaP, F-38000 Grenoble, France
[d] ElyTMaX IRL3757, CNRS, Université de Lyon, INSA Lyon, Centrale Lyon, Université Claude Bernard Lyon 1, Tohoku University, Sendai, 980-8577, Japan

ARTICLE INFO

Keywords:
Ti-6Al-4V
Laser Powder Bed Fusion
Heat treatments
Alpha-case
Fatigue
Embrittlement

ABSTRACT

This research investigates the effect of the formation of an oxygen-stabilised titanium alpha layer – called alpha-case at the surface – on the fatigue properties of Ti-6Al-4V (Ti64) alloy components produced by Laser Powder Bed Fusion (L-PBF). Three post processing heat treatments with different controlled atmospheres were carried out on samples with as-built surfaces to evaluate how differences in alpha-case layer thickness and hardness affect the material's susceptibility to surface embrittlement and its overall fatigue performance. The investigation includes bulk and subsurface microstructural analysis, surface characterisation by X-ray computed tomography (XCT), and fatigue testing. Key findings show that alpha-case layers can reduce the fatigue resistance of L-PBF fabricated Ti64. The presence of a 70 ± 3 µm thick alpha-case layer was found to promote crack initiation. This is emphasised by a higher density of initiated cracks, thus leading to a reduction in fatigue life. Conversely, thinner alpha-case layers were found to have a reduced impact on the fatigue performance, highlighting the critical role of post processing heat treatments in modulating the fatigue resistance of the material. The use of XCT to characterise the surfaces of the specimens in 3D confirms that fatigue cracks primarily initiate at surface notches, highlighting the predominance of as-built surfaces over microstructure in determining the fatigue resistance of L-PBF Ti64 components.

1. Introduction

Among additive manufacturing (AM) processes, Laser Powder Bed Fusion (L-PBF) stands as a prevalent method for producing metallic components [1,2], particularly in the aerospace sector, a major driver for this technology [3]. The fabrication of geometrically complex components in Ti-6Al-4V (Ti64) alloy using L-PBF has proven to be robust [4,5]. Nevertheless, the widespread adoption of Ti64 produced via L-PBF is hampered by several challenges. In particular, *as-manufactured* parts exhibit significant residual tensile stresses near their surfaces [4,6], a predominantly fine martensitic α' microstructure [7,8], together with manufacturing defects such as pores [9], and considerable surface roughness including various surface defects [10,11]. The martensitic microstructure confers high strength but results in a poor ductility [10,12,13], and in conjunction with residual stresses, adversely affects the fatigue performance of the material [14,15].

To improve the mechanical properties, post processing heat treatments (HT) are used to relieve residual stresses [16,17] and to decompose the martensitic microstructure into a balanced $\alpha + \beta$ mixture. Extensive research has been undertaken to develop HT that retain a fine equilibrium microstructure to optimise the strength/ductility trade-off of the alloy. This research has primarily focused on machined and/or polished samples [12,15,18,19], but excellent tensile properties were also found with near-net-shape samples with as-built surfaces [13,20,21].

However, fatigue properties are significantly affected by a variety of surface defects inherent to the L-PBF process [22,23]. The detrimental effect of as-built surfaces on the fatigue properties of Ti64 alloy produced by L-PBF is well documented, affecting both as-fabricated (untreated) and stress-relieved samples [24,25], sub-transus heat treatments [26], or hot isostatic pressing [27,28], each resulting in different

* Corresponding author at: Mines Saint-Etienne, Univ. Lyon, CNRS, UMR 5307 LGF, F-42023 Saint-Etienne, France.
E-mail address: quentin.gaillard@emse.fr (Q. Gaillard).

https://doi.org/10.1016/j.ijfatigue.2024.108621
Received 11 June 2024; Received in revised form 20 September 2024; Accepted 21 September 2024
Available online 26 September 2024

microstructural characteristics. These defects act as stress concentrators, facilitating local plastic deformation and potentially leading to crack initiation early in the fatigue life. Such surface defects significantly reduce the fatigue strength by accelerating the crack initiation stage. In particular, Ti64 alloys produced by additive manufacturing are particularly sensitive to notch-like surface defects [29–31], which can originate from various sources. In up-skin and vertical regions, these defects may be caused by the layering of molten powder, often resulting in a plate-pile or staircase-like surface appearance [29,32,33]. Crack initiation on Ti64 as-built surfaces inherited from L-PBF most commonly occurs at surface notches [23–26]. Various studies have shown that notches are the primary origin of failure in most cases for both L-PBF and E-PBF Ti64 samples with as-built surfaces [24,25,27].

When exposed to high temperatures in an oxygen-containing environment, such as during HT performed in air, titanium and its alloys are susceptible to the formation of oxide layers on the surface. This goes hand in hand with oxygen diffusion from the surface into the bulk of the material [34,35]. The oxygen-enriched layer, commonly referred to as "alpha-case", is characterised by its high hardness and brittleness and is often associated with a decrease in mechanical properties, primarily due to the initiation of surface cracks under load [36,37]. To date, few studies have specifically investigated the effect of the brittle alpha-case on the fatigue properties of titanium alloys. On a mill-annealed $\alpha + \beta$ alloy with an equiaxed microstructure, Fukai et al. revealed that the bending fatigue strength ($R = -1, f = 25$ Hz) deteriorates in the presence of an alpha-case layer approximately 50 μm thick [38]. In addition, Pilchak et al. found that the fatigue life ($R = 0.05, f = 20$ Hz) of a heat-treated near-α alloy with an equiaxed microstructure is severely reduced by a factor of 10 with an alpha-case layer of approximately 35 ± 5 μm [39]. Gaddam et al. demonstrated that the low cycle fatigue life ($R = 0, f = 0.5$ Hz) of a heat treated near-α alloy with a bimodal microstructure decreases by 50% and 90% at a strain amplitude of 0.4 %, with alpha-case layers of approximately 2 μm and 10 μm, respectively [34]. Traditional manufacturing routes for titanium products, such as casting and forging, usually involve a machining step on the heat treated ingot or semi-finished product. The alpha-case layer formed during fabrication and/or HT is therefore removed at this stage. Conversely, in the case of L-PBF products used in near-net-shape (no surface treatment), an alpha-case layer can potentially form during the post-fabrication HT. Recently, it has been shown that the ductility of L-PBF produced Ti64 is affected by alpha-case layers with depths ≥ 50 μm [13]. However, to the best of our knowledge, the effect of the alpha case on the fatigue properties of Ti64 components produced by L-PBF has not been investigated. It is worth noting that L-PBF Ti64 has specific characteristics compared to the aforementioned studies, such as printing defects, high surface roughness and fine microstructure.

As the fatigue strength of Ti64 components is often critical in aerospace applications [40], a major challenge in manufacturing them by L-PBF is to improve the surface quality. Post processing surface treatments have been shown to significantly improve fatigue resistance [22,26,41]. However, the applicability of many surface treatments may be limited by cost or feasibility, particularly for parts with complex geometries or internal features. Therefore, in cases where HT induces an alpha-case layer on the surface of L-PBF Ti64 specimens that cannot be mitigated by surface treatment techniques, a negative effect on fatigue properties is expected. The purpose of this study is to evaluate the influence of different heat treatment conditions on the thickness of the alpha-case layer and to assess the effect of such oxygen-enriched layers on the fatigue life of parts with as-built surfaces.

2. Materials and experimental methods

2.1. Samples manufacturing

The specimens examined in this study were produced in near-net-shape using a first generation AddUp FormUp 350 machine operated by the French aerospace manufacturer Dassault Aviation in Argonay, Savoie, France. This machine is equipped with two YAG lasers, each with a power of 500 W and operating at a wavelength of 1 070 nm. The build plate was divided equally between the two lasers, each covering half of the build area. A laminar flow of argon (Ar) was used to maintain a controlled atmosphere within the build chamber. Powder deposition was achieved using a roller mechanism. The build plate was not preheated prior to the build process. The scanning strategy involved applying a meander scan pattern and alternating the laser vectors by 90° between successive layers. Due to confidentiality agreements, specific details of other parameters remain undisclosed. The material used for the samples was ASTM Ti64 Grade 5 powder, supplied by TEKNA, Canada, and produced by plasma atomisation. The powder, whose chemical composition is given in Table 1, had a particle size distribution ranging from 5 μm to 25 μm.

Table 1
Chemical composition of the batch of grade 5 Ti64 powder used in this work.

	Ti	Al	V	Fe	O	C	N	H
wt%	Base	6.22	3.87	0.18	0.14	0.009	0.02	0.004
at%	Base	10.49	3.46	0.15	0.40	0.03	0.07	0.18

The samples investigated in this study are cylindrical fatigue specimens with a gauge length of 3 mm, a diameter of 3 mm (see Fig. 1.a for further details) and with their longitudinal direction parallel to the build direction. Whilst the use of a roller facilitates the creation of a dense powder bed, care must be taken when producing slender elements to prevent the displacement of freshly deposited thin layers by the action of the roller. Consequently, as shown in Fig. 1, the production of vertical specimens required the use of "sarcophagus-like" support structures: Fig. 1.b shows the two halves of the support structure with the vertical fatigue specimen still inside and maintained, while Fig. 1.c shows a similar fatigue specimen outside the support structure along with one half of it.

It should be noted that the supports were designed to closely surround the specimens without making direct contact with the cylindrical section of the gauge. These structures helped to stabilise the powder bed and prevented the specimens from bending in the direction of the roller. After fabrication, the build plates underwent a cleaning process in a water-filled ultrasonic bath, a critical step to remove any remaining loose powder particles. Therefore, the support structures are designed with powder extraction holes to help remove any powder remaining between the supports and the specimens at this stage (see Figs. 1.b and 1.c). In order to preserve the original surface characteristics and to avoid hiding defects such as notches, the build plates and attached specimens were not sandblasted.

2.2. Heat treatment conditions

Prior to removing the samples from the base plate, a stress relieving HT at 720 °C for 2 h was applied to the entire build plate. This procedure was designed to mitigate the potential deformation that could occur if the samples were removed prior to stress relief. Preliminary studies showed that this HT effectively eliminated the residual stresses introduced during L-PBF [16]. This HT was carried out in an industrial BMI B84T horizontal gas quenching furnace following a thermal cycle under secondary vacuum at 10×10^{-4} mbar. The cycle included heating at a rate of 10 °C/min and annealing for 2 h. This was followed by controlled cooling in the furnace at an average rate of 2 °C/min to allow the diffusion of alloying elements. Once 400 °C is reached, atomic diffusion is too slow to cause additional phase transformation, so argon was introduced into the chamber to increase the cooling rate. This stress relief HT is also described in Ref. [13], where exactly the same parameters and equipment specifications were used. Therefore, the corresponding time–temperature/pressure curves can be found in Ref. [13].

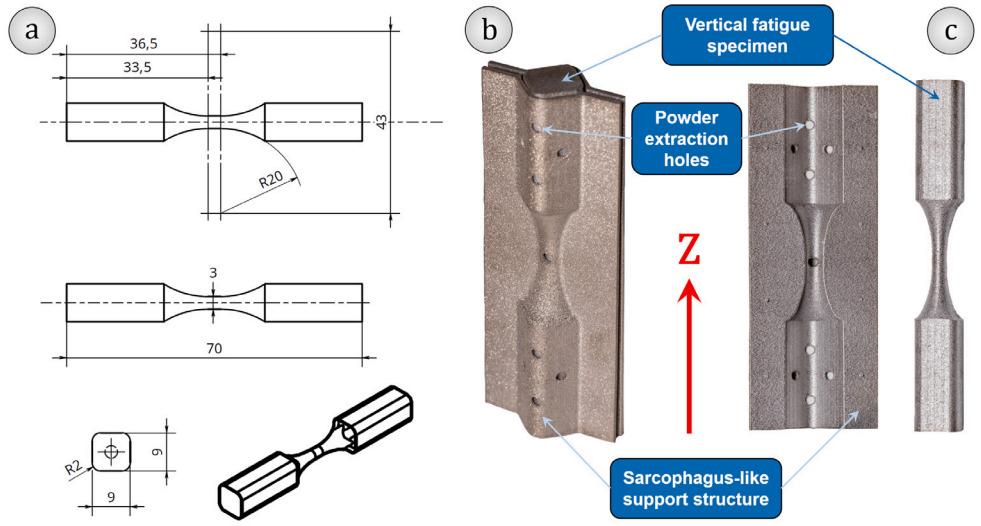

Fig. 1. Schematic dimensions of cylindrical fatigue specimens given in mm (a). Images of a vertically printed fatigue specimen inside (b) and outside (c) its sarcophagus-like support structure after cutting from the build plates.

The specimens were then removed from the build plate and the support structures were manually removed. A final ultrasonic bath was used to remove any residual powder particles between the specimens and the supports. The specimens were then divided into three groups, each subjected to different HT conditions:

- **Stress-Relieved (SR)** condition. After stress-relieving HT at 720 °C for 2 h, the first group of samples was tested without any further HT.
- **Laboratory Furnace Heat Treatment (LF-HT)** condition. Following the initial stress-relieving HT, the second group underwent an additional HT at 860 °C/4 h in a Nabertherm RHTC 80-450/15 tubular vacuum furnace. This cycle, carried out under a primary vacuum of 10×10^{-2} mbar, included heating at 10 °C/min, annealing for 4 h, and controlled cooling at an average rate of 4 °C/min. Similar to the other conditions, rapid cooling was initiated at 400 °C by water quenching.
- **Industrial Furnace Heat Treatment (IF-HT)** condition. The third group was subjected to the same HT at 860 °C/4 h after the initial stress relief, using the same industrial furnace. The parameters and thermal cycle were similar to the LF HT.

The laboratory furnace and the industrial furnace used for the additional HT are similar to those described in a previous paper [13]. In this earlier study it was observed that alpha-case formation occurred during IF-HT whereas LF-HT did not result in alpha-case formation. It was concluded that the vacuum level is not the only parameter to consider in preventing alpha-case formation at the surface of the specimens. Several factors such as the global specific surface area of the heat-treated parts and the dimensions of the chamber can also play a significant role. The industrial furnace has a much larger effective capacity (0.25 m^3) than the laboratory furnace (5×10^{-3} m^3) which can make it more difficult to maintain air-tightness. In addition, the degassing of fibre/wool insulation elements in the oven may influence oxidation during HT, thereby facilitating the formation of alpha-case. Finally, the formation of alpha-case can be influenced by the "contamination" of the industrial furnace, which is not fully dedicated to the heat treatment of titanium parts. This distinction between IF-HT (alpha-case formation) and LF-HT (no alpha-case formation) allowed a comparative analysis to distinguish the effects of microstructural changes from the effects of alpha-case, both outcomes depending on the HT temperature. The results can be extended to the material studied in the present work, since the samples used in the previous study were produced with the same Ti64 powders, L-PBF machine, process parameters and underwent HT under the same conditions.

The HT at 860 °C/4 h was selected based on its ability to achieve an equilibrium $\alpha + \beta$ microstructure, which is known to enhance the strength-ductility trade-off of this alloy [12,13,42]. Furthermore, in our previous study, it was found that alpha-case formation reduced the overall ductility and the elongation to failure of the alloy when subjected to HT for 2 h at 860 °C or higher [13]. Consequently, a similar temperature range was adopted in the current study to assess the effect of alpha-case formation on the fatigue performance of the material.

2.3. Microstructure characterisation

Microstructural analysis was performed using Optical Microscopy (OM) and Scanning Electron Microscopy (SEM). After the fatigue tests, samples were prepared from the gauge length of the specimens, including both horizontal (XY) and vertical (Z) cross sections. Preparation for microstructural examination involved grinding the specimens with 320 grit SiC paper followed by polishing with a 9 µm diamond solution. This was followed by chemical and mechanical polishing using a mixture of 50 nm colloidal silica suspension (90%), hydrogen peroxide (6%) and ammonia (4%). For microstructure imaging by Backscattered Electron (BSE) or Electron Backscattered Diffraction (EBSD), the samples were further polished by vibratory polishing with colloidal silica.

Area phase fractions were quantified from BSE images acquired using a ZEISS Supra 55 VP Field Emission Gun SEM. Image analysis, performed using ImageJ software, allowed phase discrimination based on the contrast observed in the images. This analysis provided the average phase fraction (± standard deviations) from 20 images taken in the XY plane for each HT condition. EBSD analysis was performed using the same SEM operating at 20 kV with an Oxford Instruments Symmetry camera. For each condition an EBSD map was collected with a step size of 0.25 µm in the XY plane. The EBSD data were processed using the MTEX toolbox in MATLAB, identifying α lath boundaries with a 5° misorientation threshold between grains. Grains smaller than 10 pixels were excluded from the analysis and the thickness of the α laths was determined by fitting ellipses and measuring the minor axis.

The alpha-case layer on samples polished in the XY plane was revealed using Weck's reagent (ammonium bifluoride dissolved in ethanol and water) for approximately 30 s. Micrographs of the etched samples were taken using an Olympus GX51 light microscope. Quantitative measurements of the thickness of the alpha-case layer were made using ImageJ software, based on 20 images taken around the perimeter of the specimen.

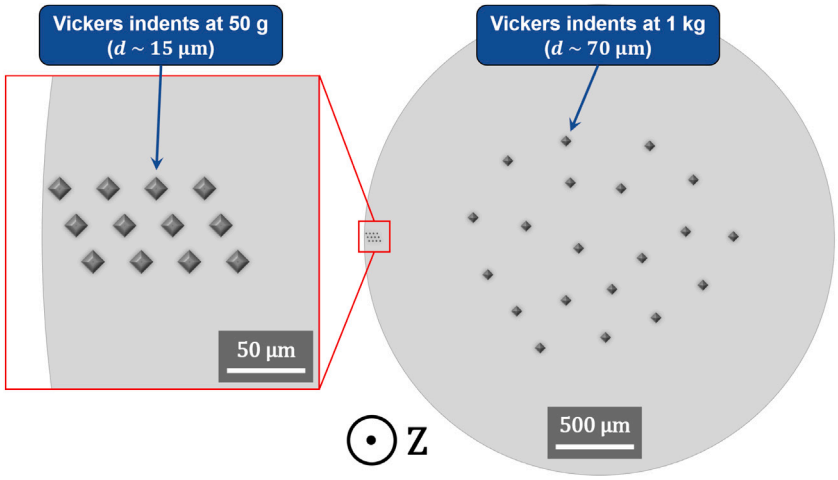

Fig. 2. Schematic representation of the locations of the Vickers hardness measurements made at 50 g and 1 kg on horizontal (XY) polished cross-sections of fatigue specimens.

Table 2
Microstructural characteristics and bulk hardness measurements for the three HT.

Condition	α laths thickness (µm)	β phase fraction (%)	Bulk hardness (HV1)	Alpha-case thickness (µm)
SR (720 °C/2 h)	0.61 ± 0.05	2.2 ± 0.3	395 ± 2	10 ± 1
LF-HT (SR + 860 °C/4 h)	1.02 ± 0.07	4.2 ± 0.4	368 ± 2	–
IF-HT (SR + 860 °C/4 h)	1.06 ± 0.08	4.1 ± 0.3	366 ± 3	70 ± 3

2.4. Mechanical tests

Fatigue tests were conducted in air at room temperature using an Instron 8516 servo-hydraulic machine equipped with a 100 kN load cell. These tests were performed at a constant stress amplitude, using a sinusoidal waveform at a frequency of 10 Hz, with the stress ratio set at $R = 0.1$. A range of maximum applied tensile stress between 300 MPa and 650 MPa was selected from the fatigue properties found in the literature for L-PBF Ti64 with as-built surfaces. A total of 23, 9, and 14 specimens were tested for the SR, LF-HT and IF-HT conditions respectively. Tests that did not result in failure after 10^7 cycles for SR specimens were stopped and classified as "run-outs". Due to time constraints, run-out LF-HT and IF-HT specimens were only stopped after 1.5×10^6 cycles. For each condition, one specimen subjected to a maximum applied stress of 450 MPa was cycled for approximately 95% of its estimated life and then removed from the fatigue machine unbroken. These specimens are hereafter referred to as "interrupted". The stresses were determined based on the theoretical initial cross-sectional area, $S = \pi \frac{(3\ \text{mm})^2}{4} \approx 7.07\ \text{mm}^2$.

Vickers microhardness tests were performed on horizontal (XY) mirror-polished cross-sections of fatigue specimens using a Buehler microhardness tester. To determine the bulk hardness for the three conditions studied, 20 measurements were taken at random locations within the bulk of the samples, as shown schematically in Fig. 2. These bulk measurements were taken using a load of 1 kg and an indentation time of 15 s, resulting in an average indentation diagonal length of 70 µm. The results are presented in Table 2 as means ± standard deviations.

In addition, to assess the increase in hardness due to the oxygen enriched alpha-case layer, microhardness profiles were obtained at a load of 50 g, resulting in an average indentation diagonal of 15 µm. This load was chosen to minimise the effects of microstructural variability, thereby reducing data scatter whilst maintaining adequate spatial resolution. The initial indentation was placed at 10 µm from the sample surface and measurements were taken in a staggered pattern to achieve a spatial resolution of 10 µm between successive points, as shown in the enlarged view of Fig. 2. Three hardness profiles were obtained for each condition and the results are shown in Fig. 5.b as a curve representing the data together with the scatter plots of each measurement.

2.5. 3D characterisation of surfaces using X-ray computed tomography

X-ray computed tomography (XCT) was used to scan the gauge length of all the fatigue specimens, both before the fatigue test and after fatigue failure. The scans were performed using a cone beam phoenix | X-ray V | tome | x laboratory tomograph, set to a voltage of 140 kV and a current of 80 µA, capturing 1200 projections. A 0.1 mm Cu filter was implemented to minimise beam hardening artefacts during acquisition. After acquisition, the images were processed with a 3×3 median denoising filter. Image reconstruction was performed using a standard filtered back-projection algorithm supported by the proprietary phoenix datos|x software. In addition, a numerical filter was applied during reconstruction to further reduce beam hardening artefacts.

Each specimen was scanned three times along its longitudinal axis prior to fatigue testing with a small overlap of 100 µm. The number of scans was chosen primarily to ensure that failure always occurred in an area previously characterised by XCT. The voxel size for each sample was 3 µm, with a total characterised length from the three scans of 11 mm. After reconstruction, the scans were converted to 8-bit unsigned volumes and merged using a custom Python script. To reduce noise, a $2 \times 2 \times 2$ median filter was applied to the aggregated volume. This processed volume was then used to compute local surface roughness and curvature, as inherited from the L-PBF method. The methodology for calculating these parameters to achieve 3D characterisation of complex surfaces is described in detail in Ref. [43].

XCT scanning of the fatigue specimens enabled the characterisation of the as-built surfaces using the aforementioned *ex situ* methodology, both before and after fatigue testing. The derived data supported a comprehensive killer defect identification workflow. This workflow involves analysis of the fracture surface of fatigue specimens using SEM in Secondary Electron (SE) or Backscattered Electron (BSE) mode to locate the crack initiation site. It then involves the study of the 3D fracture surface from XCT scans taken after fatigue failure and the identification of the killer defect on the 3D surface from the XCT scan of the pre-fatigue specimen [43,44].

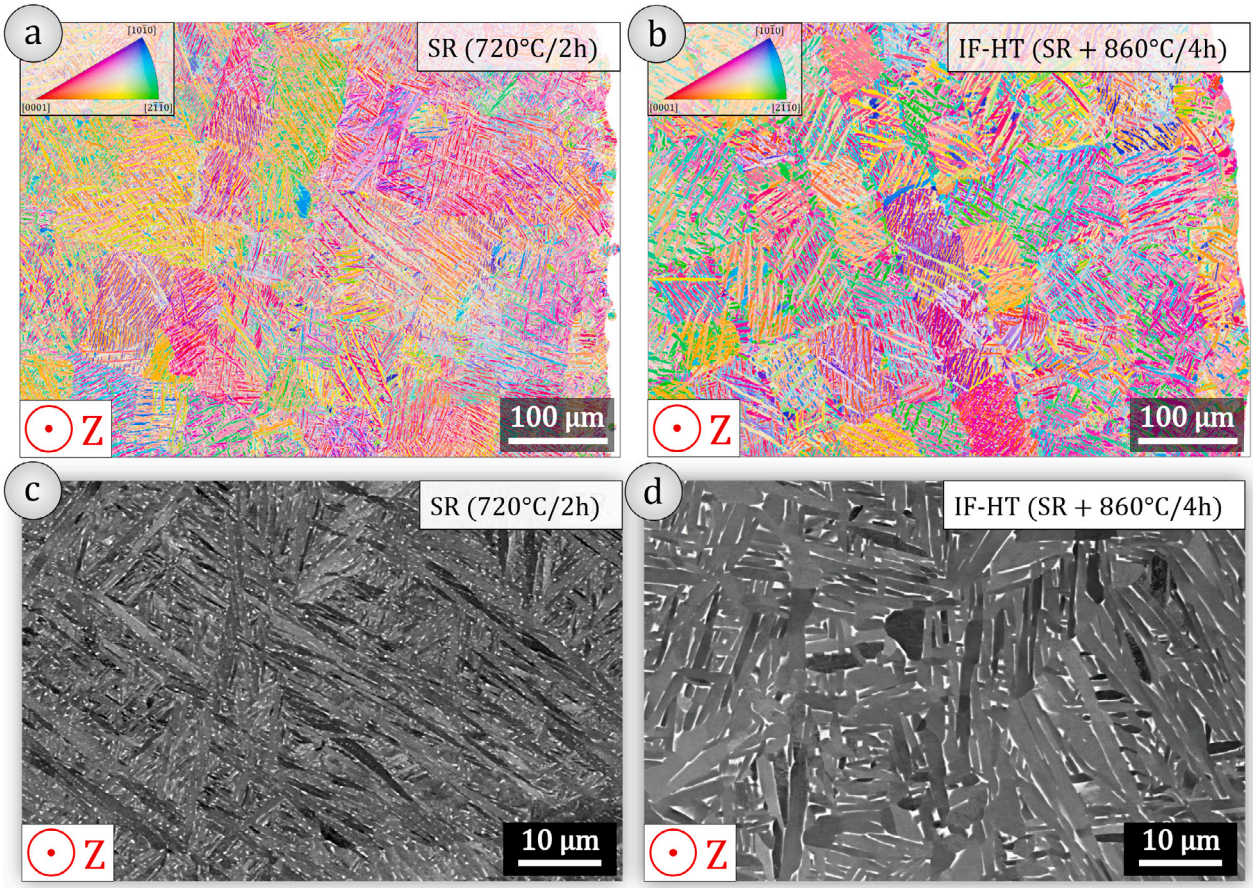

Fig. 3. EBSD inverse pole figure α orientation maps (a and b) and SEM-BSE images (c and d) showing the microstructure of an SR (720 °C/2 h) sample (a and c) and of an IF-HT sample (720 °C/2 h + 860 °C/4 h) (b and d). In the EBSD maps, the build direction Z is used as the reference axis. In the SEM-BSE images, the α phase appears in dark contrast, while the β phase appears in white.

3. Results and discussion

3.1. Bulk microstructure observations

Fig. 3 shows EBSD inverse pole figure maps of the α phase (Figs. 3.a and 3.b), alongside SEM-BSE images (Figs. 3.c and 3.d). Each image was taken in a plane perpendicular to the building direction Z.

Each HT condition is characterised by a two-phase $\alpha+\beta$ microstructure (α, hexagonal close-packed and β, body-centred cubic). This microstructure results from the decomposition of the as-built α' martensitic phase during post processing heat treatment at annealing temperatures above 500 °C [45,46]. The α' martensite forms on cooling from the parent β grains. In planes normal to Z, the legacy structures from the parent β grains create a "chessboard pattern", as seen in Figs. 3.a and 3.b. Such patterns are typically observed in Ti64 produced by L-PBF using a 0°/90° scanning strategy between layers [7,47,48]. As up to 12 different α variants can form from a single parent β grain orientation [16,49,50], this contributes to the randomisation of the texture of the α phase as shown in Figs. 3.a and 3.b. The α laths thicknesses were measured from EBSD orientation maps similar to those shown in Fig. 3.a for the SR condition and Fig. 3.b for the IF-HT condition. The average α laths thickness was estimated and the results are summarised in Table 2. In the SR condition, the α laths thickness is 0.61 ± 0.05 µm. These values are slightly higher than those reported in Ref. [13] for the same material using the same method. This is due to the use of a larger EBSD step size which reduces the detection of ultra fine α laths. After LF-HT and IF-HT the α laths are thicker, averaging 1.02 ± 0.07 µm and 1.06 ± 0.08 µm respectively. These values are close to the average α lath thickness reported in the literature for similar HT conditions [42,51].

SEM-BSE images, similar to those shown in Fig. 3.c for the SR condition and Fig. 3.d for the IF-HT and LF-HT conditions, allowed the estimation of the α/β phase fractions, with the results summarised in Table 2. In the SR condition, the β phase fraction barely reaches 2.2 ± 0.3 %, but almost doubles after LF-HT or IF-HT to 4.2 ± 0.4 % and 4.1 ± 0.3 %, respectively.

In summary, the bulk microstructure of the Ti64 alloy in the SR condition consists of finer α lamellae and a lower β phase fraction compared to the bulk microstructure after additional HT at 860 °C/4 hours. The bulk microstructures resulting from LF-HT and IF-HT are almost identical. This correlates with the bulk hardness measurements for each condition as shown in Table 2. The material shows a higher hardness in the SR condition (395 ± 2 HV1) compared to the hardness measured after 860 °C/4 hours, regardless of the furnace used: LF-HT (368 ± 2 HV1) or IF-HT (366 ± 3 HV1).

3.2. Alpha-case characterisation

The alpha-case layers identified in the three HT conditions are shown in Fig. 4. The use of Weck's reagent selectively highlights the oxygen rich layer in white, making it easier to measure the thickness of the alpha-case layer. The measurements are given in Table 2.

For the SR condition (Fig. 4.a), a 10 ± 1 µm thick alpha-case layer was revealed after etching, in agreement with the results reported in Ref. [13] for the same condition in the industrial furnace.

Despite the similar initial SR treatment, the LF-HT condition showed no discernible alpha-case layer (Fig. 4.b). This can be attributed to the diffusion of oxygen from the initial alpha-case layer formed during SR deeper into the material during the subsequent treatment at 860 °C/4 h,

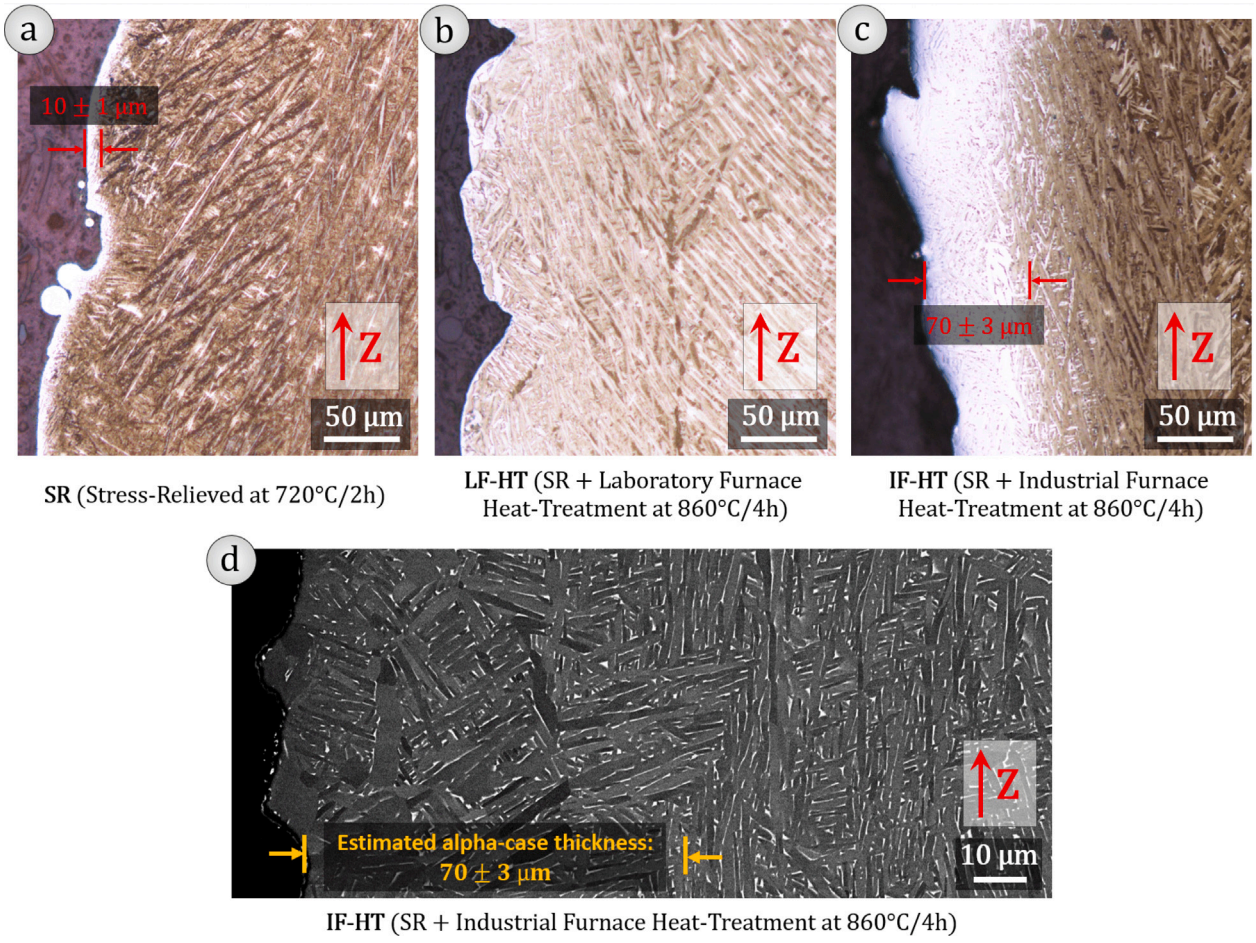

Fig. 4. Characterisation of the alpha-case in SR (a), LF-HT (b) and IF-HT (c) conditions. These optical micrographs, taken from vertical (Z) cross-sections of fatigue specimens, reveal the alpha-case in white after chemical etching using Weck's reagent. SEM-BSE image (d) showing the surface microstructure of an IF-HT specimen.

resulting in its diffusion within the core material. This implies that no additional oxygen was introduced into the alloy in the laboratory furnace atmosphere, a conclusion also drawn in the aforementioned study [13].

In the IF-HT scenario, the initial 10 ± 1 µm-thick alpha-case layer expanded to 70 ± 3 µm due to enhanced oxygen diffusion from the specimen surface in the oxidising environment of the industrial furnace (Fig. 4.c). Compared to the alpha-case layers documented in the previous study, this 70 ± 3 µm measurement at 860 °C/4 h falls between the values obtained for IF-HT at 860 °C/2 h (48 ± 2 µm) and 920 °C/2 h (90 ± 5 µm) [13]. This observation is consistent with the understanding that alpha-case formation in Ti64 alloy produced by L-PBF is primarily dependent on the HT temperature and is driven by the diffusion of oxygen in α titanium [13,35].

Finally, Fig. 4.d shows an SEM-BSE image taken at the surface of an IF-HT specimen. In the region of the estimated alpha-case thickness ($\approx 70 \pm 3$ µm from Fig. 4.c), a gradient of β phase area fraction can be seen: almost no β is found near the surface (only isolated islands of β phase appearing in bright contrast), then the β phase becomes more visible with a more elongated morphology with increasing depth. Beyond the alpha-case thickness, the bulk microstructure already observed in Fig. 3.d is found. This gradient in the β phase area fraction can be attributed to the presence of an oxygen content gradient from the surface. Indeed, oxygen is a strong alpha-forming element in titanium alloys, thus reducing the stability of the β phase. Oxygen gradients at the surface will be further discussed in the next paragraphs.

Fig. 5.a shows microhardness profiles taken from the surfaces of horizontal (XY) polished cross-sections of fatigue specimens under the three different conditions (see indent locations in Fig. 2). The scatter plots for the three measurements taken at different depths are shown, together with the fitted curve (dashed line) for each condition.

For the SR condition, a marginal increase in hardness is observed at a distance of 10 µm from the surface, with subsequent measurements closely matching the bulk hardness detailed in Table 2. In the LF-HT condition, the initial hardness measured at 10 µm from the surface exceeds the bulk hardness and shows a gradual decrease as one moves towards the bulk. Conversely, the IF-HT condition shows a significant increase in hardness, with mean values remaining above 400 HV0.05 up to a depth of 70 µm from the surface.

The observed increase in hardness is associated with an increase in oxygen concentration, a correlation supported by numerous studies [37,52,53]. To estimate the oxygen content corresponding to these hardness measurements, oxygen diffusion profiles were modelled based on the solution of Fick's second law for a semi-infinite solid (Eq. (1)). This model assumes a steady-state concentration C_S at the surface, a uniform initial concentration C_0 within the bulk, and a constant diffusion coefficient D which can be calculated using an Arrhenius law under isothermal conditions (Eq. (2)) [35,54,55].

$$C(x,t) = C_0 + (C_S - C_0) \times \left(1 - erf\left(\frac{x}{2\sqrt{Dt}}\right)\right) \quad (1)$$

$$D(T) = D_0 \times \exp\left(\frac{-Q}{RT}\right) \quad (2)$$

The pre-exponential factor D_0 and the activation energy Q were set to 1.31×10^{-3} m^2 s^{-1} and 225.8 kJ mol^{-1} respectively. These values correspond to the experimentally determined oxygen diffusion coefficients in the same L-PBF Ti64 alloy from the previous study [13]. They

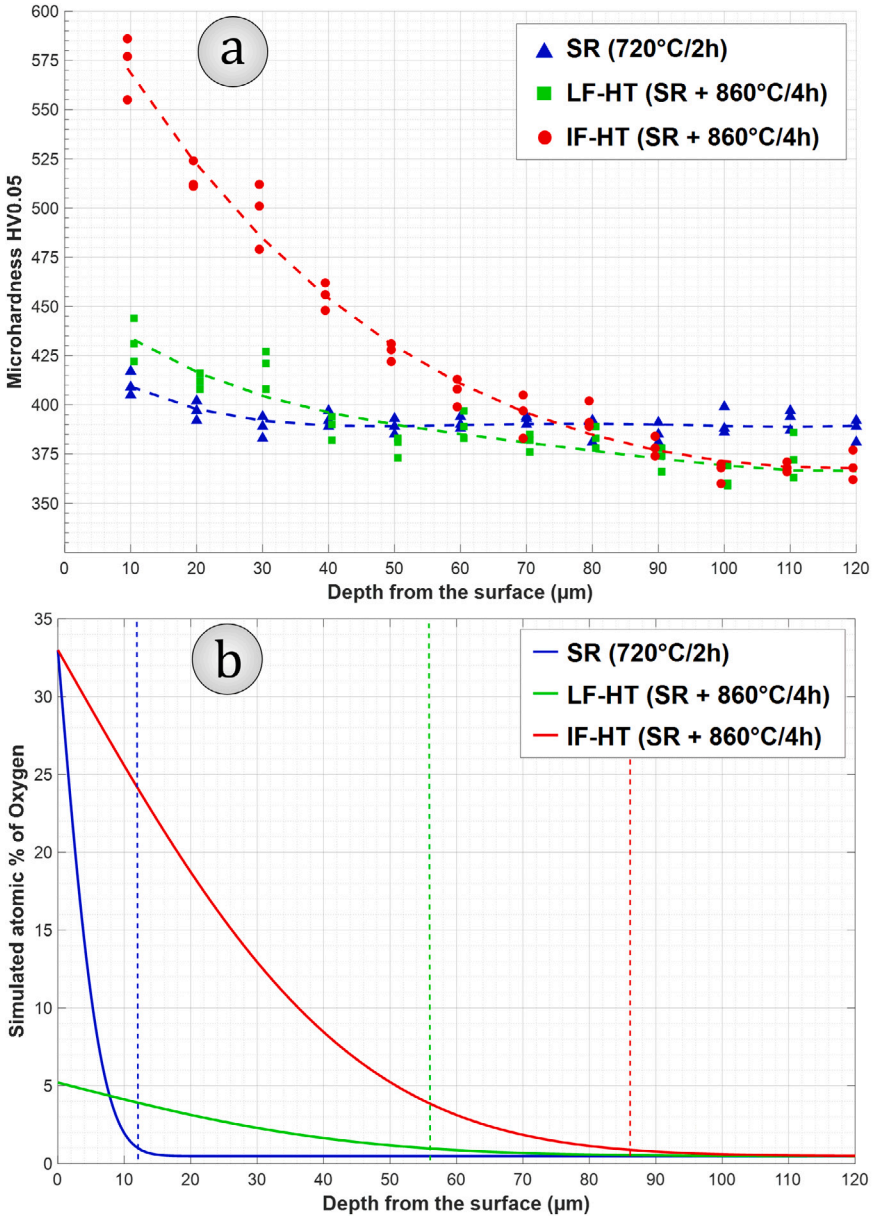

Fig. 5. Microhardness (HV0.05) profiles (a) and simulated oxygen concentrations (b) for fatigue specimens under SR, LF-HT, and IF-HT conditions. Microhardness data and simulated oxygen concentration gradients are plotted against the depth from the surface. Vertical dashed lines mark the depths at which an oxygen concentration of 1 at% is reached.

are close to those found in the literature for oxygen diffusion in L-PBF Ti64 [35] or in α titanium [56]. The initial concentration parameter C_0 was set to 0.48 at%, corresponding to the bulk material concentration as determined by infrared absorption analysis of combustion gas with a LECO TC-436 (O,N) analyser. This value is slightly higher than the 0.40 at% reported in Table 1 for the powder batch used in this work. In fact, it was reported in Ref. [45] that oxygen pick-up occurs during L-PBF. For both SR and IF-HT conditions, the surface concentration C_S was set to 33 at%, reflecting the maximum solubility limit of oxygen in the titanium α phase. Using these parameters in Eqs. (1) and (2), the oxygen concentration profiles for the SR and IF-HT conditions (blue and red solid lines, respectively) were simulated and are shown in Fig. 5.b. For the LF-HT condition, it is hypothesised that the oxygen initially absorbed into the alpha-case layer during the SR treatment further diffused into the material during the LF-HT treatment without any additional oxygen intake. This idea is consistent with the absence of a visible white alpha-case layer on LF-HT samples after etching with Weck's reagent, as shown in Fig. 4.b. Consequently, when modelling the oxygen concentration profile for the LF-HT condition, the surface concentration parameter C_S was adjusted to ensure that the total oxygen content (represented by the area under the curve) was consistent between the SR and LF-HT conditions. This adjustment resulted in a C_S value of approximately 5.2 at% and allowed the green solid line profile to be plotted on Fig. 5.b. Based on the simulation, the oxygen content at the extreme surface (depth 5 µm) is significantly reduced for the LF-HT condition compared to the SR condition, but higher from 10 µm depth from the surface. However, in the first 70 µm from the surface, the oxygen concentration is much lower for the LF-HT condition compared to the IF-HT condition. In each simulated oxygen concentration profile, vertical dashed lines mark the depths at which an oxygen concentration of 1 at% is reached. This threshold indicates the level of oxygen above which the ductility of Ti64 decreases significantly [57,58]. Finally, when the fitted microhardness data profiles (Fig. 5.a) are compared with the simulated oxygen concentration profiles (Fig. 5.b) between 10 µm and 120 µm depths from the surface, a good correlation is found.

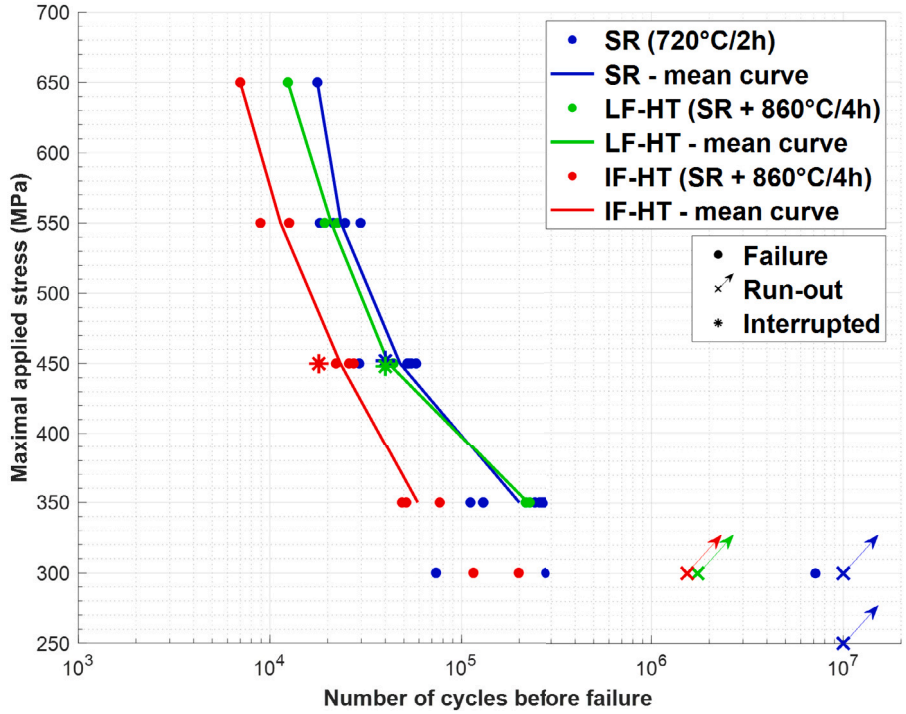

Fig. 6. Wöhler curves for SR, LF-HT and IF-HT conditions. Fatigue tests are performed at $R = 0.1$. The straight lines correspond to the mean curves that cross each mean value of the number of cycles before failure for the different applied stresses.

3.3. Fatigue properties

Fig. 6 shows the Wöhler (S-N) curves for the three conditions evaluated. Each data point, classified by different markers, illustrates the result for a tested specimen. The markers (circles, crosses, stars) correspond to three possible scenarios: failure, test interruption or survival for the duration of the test (run-out). The solid lines represent the average trend lines, each intersecting the average number of cycles to failure at different maximum applied stresses.

The plot shows no noticeable difference in fatigue resistance between the SR and LF-HT conditions. Firstly, this suggests that the microstructural changes resulting from the LF-HT at 860 °C/4 hours have a limited effect on fatigue resistance. Secondly, it questions the real effect of the 10 µm alpha case layer found on the SR samples. However, a reduction in fatigue life is demonstrated for the IF-HT condition at maximum applied stresses greater than 350 MPa. The microhardness profiles shown in Fig. 5.a suggest that the alpha-case layer increases brittleness, a phenomenon more evident in the IF-HT condition which developed a 70 µm thick alpha-case layer during industrial heat treatment at 860 °C/4 hours (Figs. 4 and 5.a). Our previous study reported that alpha-case layers ≥ 50 µm reduce the elongation to failure of near-net-shape Ti64 samples produced by L-PBF [13]. The present study further confirms that such alpha-case layers also negatively affect the fatigue resistance of L-PBF Ti64 specimens.

In this study the fatigue strength at 10^7 cycles is estimated to be around 250 MPa. As expected, the scatter of fatigue life increases as the fatigue strength is approached, making the fatigue properties more sensitive to small variations in defect size and harmfulness.

Despite the differences observed between the IF-HT condition and the SR and LF-HT conditions, the Wöhler curves for all three conditions are consistent with the fatigue strengths reported in the literature for specimens with as-built surfaces, typically ranging from 200 to 300 MPa [22,23,27,59,60]. In contrast, the average fatigue properties for L-PBF Ti64 specimens with machined and polished surfaces, which are significantly higher, typically range between 400 and 600 MPa [22,24,27,44,59–61]. It is therefore essential to evaluate the impact of the as-built surface state on the crack initiation mechanisms. This will be discussed in the next sections for all HT conditions.

3.4. Identification of killer defects and crack initiation mechanisms

In order to assess the influence of the as-built surface and the presence of alpha-case layers of different thicknesses on the fatigue properties, the fracture surfaces of the specimens were first examined by SEM. The analyses revealed that, for all the HT conditions studied, all failure initiating cracks originated from the surface, see some examples of each condition in Figs. 7a–c. Furthermore, as can be seen from the magnified views in Fig. 7, no pore was found to cause initiation in the crack initiation zone. This conclusion was indeed confirmed for all the conditions studied for all specimens tested until failure based on fracture surface observations using SEM.

XCT and SEM were used together to identify the initiation sites. This involved scanning the fatigue specimens by XCT both before and after failure. The procedure for identifying initiation sites is illustrated in Figs. 8a–d. First, the fracture surface is examined by SEM. For all specimens, the SEM observations did not allow the identification of a single, clearly localised defect that would have caused the crack to initiate. Rather, the cracks appear to initiate from extended zones, as shown in Fig. 7. In some cases, multiple initiation sites are identified on the surface, as shown in the BSE image in Fig. 8a. This scenario is common under all conditions, especially under high stresses. Having identified the main initiation site in the SEM image, the same fracture surface is then observed in 3D using XCT. This step requires the surface to be extracted from the XCT scan as shown in Fig. 8b. Then, by comparing 8a with 8b, the initiation site on the XCT fracture surface is identified. The next step is to compare the original XCT scan (taken before the fatigue test) with the XCT scan of the fracture surface to identify the surface defect responsible for crack initiation. As demonstrated in Refs. [43,44], the use of minimum curvature analysis is an efficient way to capture surface notches. Thus, for killer defect identification, surfaces were visualised using a point cloud where the colour bar represents the local minimum curvature of the surface, called κ_{min}, as illustrated in Fig. 8b–d. In these visualisations, surface notches typically appear in dark blue, indicating areas of lowest minimum curvature. These notches are perpendicular to the loading direction

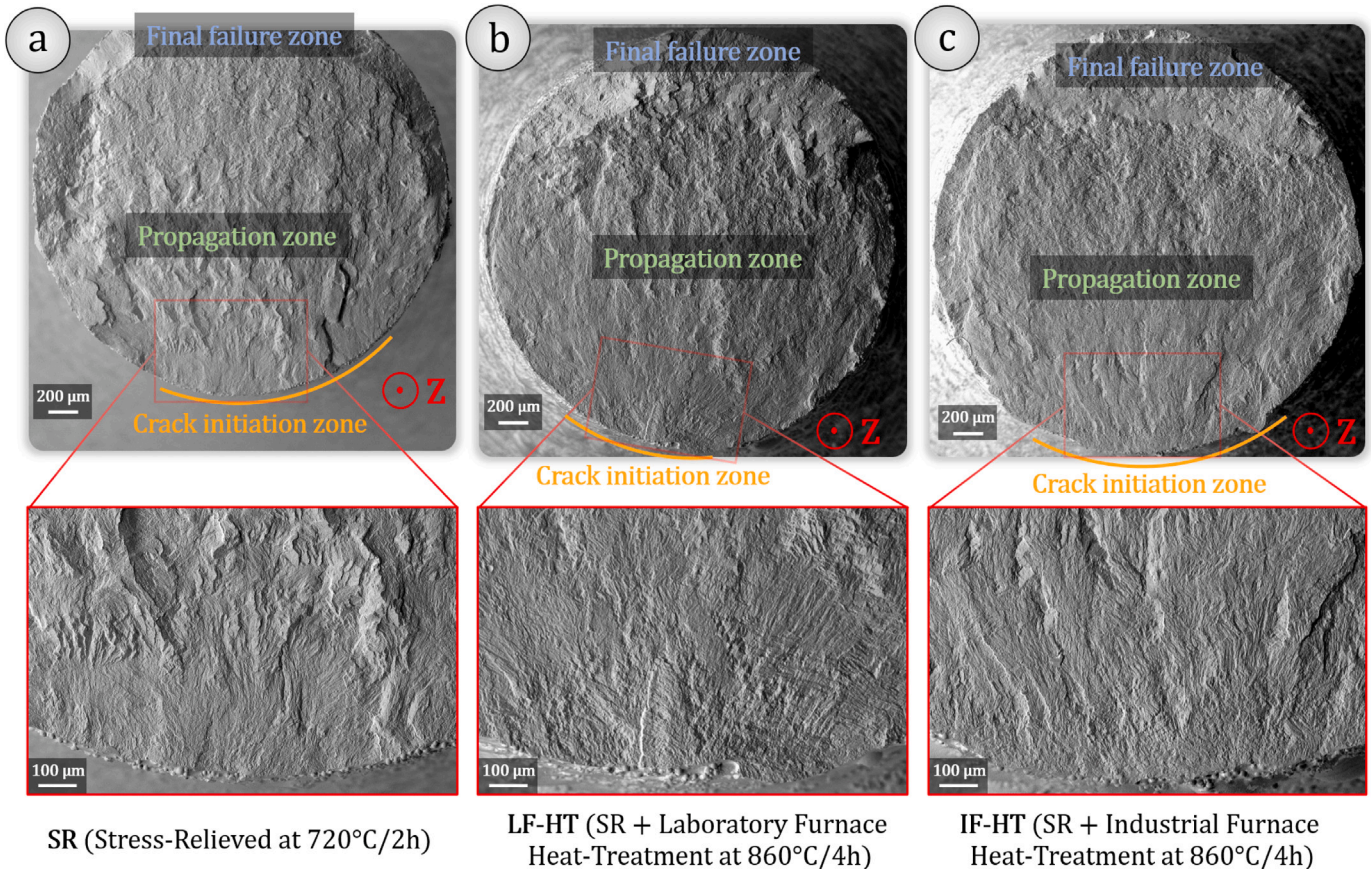

Fig. 7. SEM-BSE topological mode observation of fracture surfaces for an SR specimen that failed after 73 547 cycles at 300 MPa (a), an LF-HT specimen that failed after 40 901 cycles at 450 MPa (b), and an IF-HT specimen that failed after 198 645 cycles at 300 MPa (c). In each case, crack initiation occurs from a large portion of the surface as shown in the magnified views.

and run along the specimen surface unless interrupted by significant protrusions. Using this procedure, initiation sites were identified for 10 SR, 6 LF-HT and 6 IF-HT specimens. For 20 out of 22 specimens, failure cracks originated from plate-pile horizontal surface notches, as typically shown in Figs. 8.c-d. Remarkably, one specimen tested at σ_{max} = 450 MPa from the IF-HT condition exhibited a crack initiation site without any noticeable defect on the initial surface scanned by XCT. This situation was not observed in the SR or LF-HT specimens. This may indicate a shift in the crack initiation mechanisms due to the thicker alpha case, although it may be due to the resolution limitations of XCT, which may not capture the killer defect.

From the XCT data obtained prior to the fatigue tests, it was also possible to extract the 3D surface roughness of the 22 vertical specimens (10 SR, 6 LF-HT and 6 IF-HT) investigated. The calculation of the 3D surface roughness is described in detail in Refs. [43,44]. The roughness calculation region was performed over a length of 9 mm along the specimen axis. This includes part of the specimen fillet radius. Several roughness parameters (S_a is the arithmetic mean height, S_q the root mean square height, S_z the maximum height and S_v the maximum notch depth) were calculated and the results are summarised in Table 3. From these values, it can be concluded that the surface roughness is similar for the three conditions studied. This result suggests that the observed differences in fatigue behaviour (Fig. 6) are due to a difference in alpha case thickness and cannot be attributed to a difference in surface roughness. The mechanisms that could explain the difference in fatigue resistance in the presence of a thick alpha-case layer are discussed in Section 3.5.

The conclusion of these investigations was that the cracks initiated from shallow elongated surface notches perpendicular to the loading direction, and multiple crack initiations were observed in some specimens. On several occasions the surface crack initiation zone was found to follow the notch root, sometimes forcing it to follow a tortuous path. This illustrates well how the surface defects, particularly notches, dominate the fatigue properties of specimens with as-built surfaces. The influence of these surface notches can be explained by the stress concentration they generate at their root, also known as the notch effect. From Table 3, one can see that the calculated surface roughness parameters are similar regardless of the condition, including the maximum notch depth parameter S_v. Thus, the notch effect is expected to be the same for all fatigue specimens tested. Furthermore, the extent to which this effect affects the fatigue resistance depends on the notch sensitivity of the material. Alloys characterised by high strength and low ductility tend to have higher notch sensitivity, making them particularly susceptible to the notch effect [62]. As the mechanical properties of titanium alloys are highly sensitive to oxygen content [63], the formation of an alpha-case layer, which correlates with an increase in hardness near the surface (see Fig. 5.a), could lead to an increase in the notch sensitivity of the material near the surface, resulting in lower fatigue resistance. For example, this embrittlement could accelerate the initial phase of crack initiation.

Table 3
Roughness parameters for the specimens of the three HT, calculated from XCT data using the 3D characterisation workflow described in Refs. [43,44].

Condition	S_a (µm)	S_q (µm)	S_z (µm)	S_v (µm)
SR (720 °C/2 h)	7.2 ± 0.6	10.1 ± 0.8	143 ± 25	64 ± 20
LF-HT (SR + 860 °C/4 h)	6.7 ± 0.3	9.5 ± 0.5	137 ± 26	60 ± 11
IF-HT (SR + 860 °C/4 h)	6.9 ± 0.4	9.8 ± 0.6	129 ± 13	61 ± 10

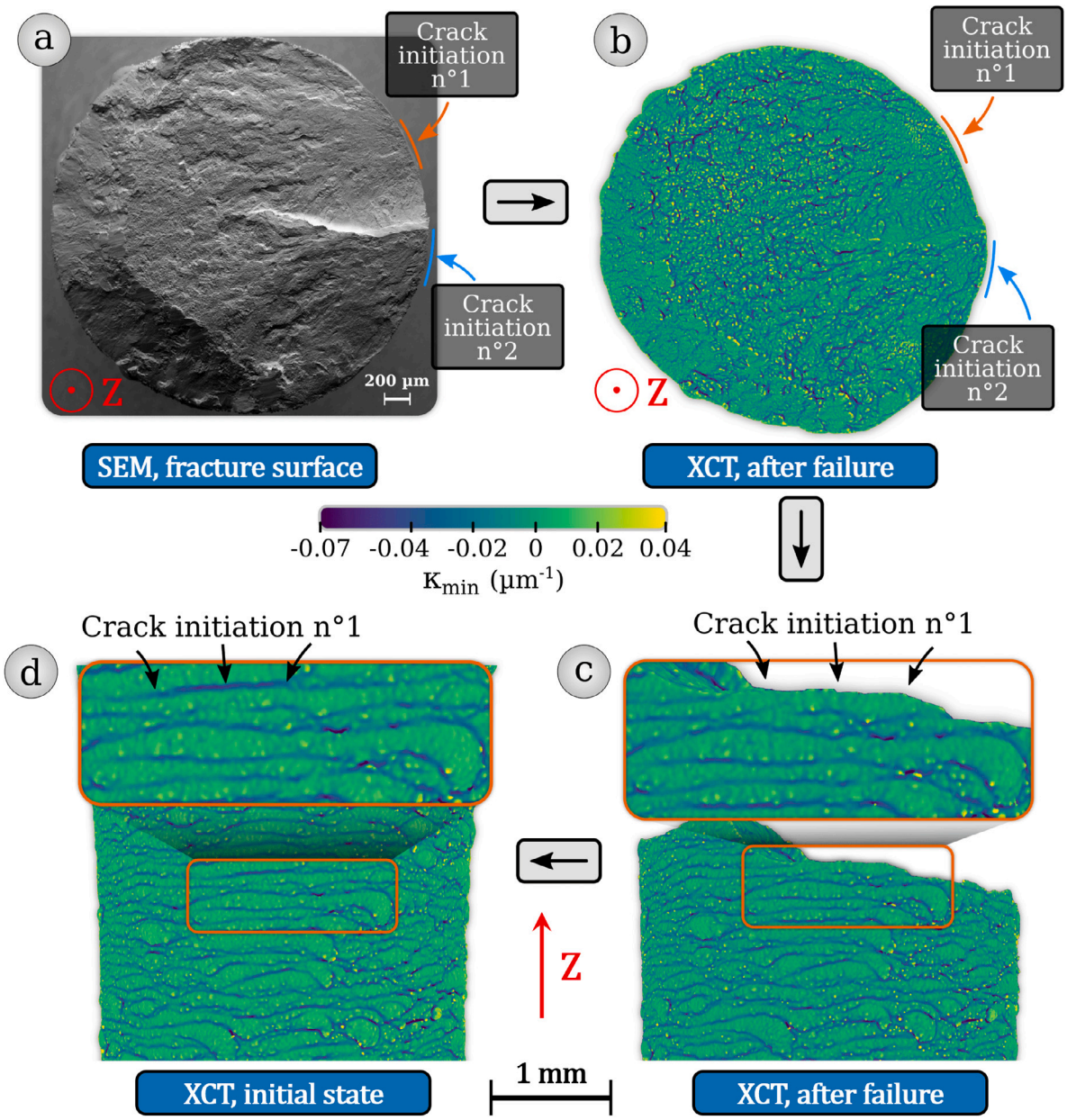

Fig. 8. Workflow for crack initiation site identification using both SEM and XCT scans. The example specimen from the SR condition failed after 129 339 cycles at 350 MPa. SEM-BSE fracture surface observation (a). Fracture surface obtained from XCT scans after failure (b). The colour bar corresponds to the minimum curvature κ_{min}, estimated by integral invariant estimation as described in Refs. [43,44]. A crack initiation site is observed on the fracture surface from the side of the specimen (c). Same area as in (c), identified from XCT scans of the initial state before the fatigue test (d). A notch is identified at the origin of the crack initiation by comparison with (c).

However, it is unclear whether there are multiple initiation sites along the notches or whether a crack initiated at one point propagates along the notch root. In attempting to answer this question, it is instructive to draw a comparison with the study by Vie et al. who investigated the effect of a 10 µm brittle alumina oxide layer on the fatigue behaviour of 7075-T6 aluminium alloy (R = 0.1) [64]. Their investigation revealed a threefold reduction in fatigue life in the presence of the oxide layer. Fig. 9 is a reproduction of an SEM fractography analysis presented in the work of Vie et al. (Figure 13 of their paper). The magnified view of the fracture surface of an anodised and polymer-coated aluminium fatigue specimen (Fig. 9.b) shows that the main crack grows from multiple crack initiation sites associated with microcracks in the oxide layer. The multiplicity of crack initiation sites results in a very large crack initiation zone as indicated by the red arrows in 9.a. In contrast, in a polymer-coated aluminium fatigue specimen with no oxide layer, the main crack propagates from a single narrow initiation site associated with intermetallic particle failure (Figs. 9.c and 9.d). These observations, coupled with in situ acoustic emission during fatigue cycling, shed light on several mechanisms for the anodised samples with the brittle alumina layer. First, multiple cracking of the oxide layer early in the fatigue life generates multiple stress concentration regions. Due to the strong adhesion between alumina and the aluminium substrate, these microcracks in the oxide layer promote multiple crack initiation into the underlying material. Second, the cracks initiated in the substrate grow and converge to form a single main crack, resulting in a large crack initiation zone. Third, cracking assisted by brittle fracture of the oxide layer makes easier the propagation of the main crack, a phenomenon referred to as the "continuous initiation process". To draw a parallel with our study, the brittle oxygen-enriched metallic layer can be compared to the oxide layer in Vie et al.'s work. Furthermore, Fig. 8 highlights

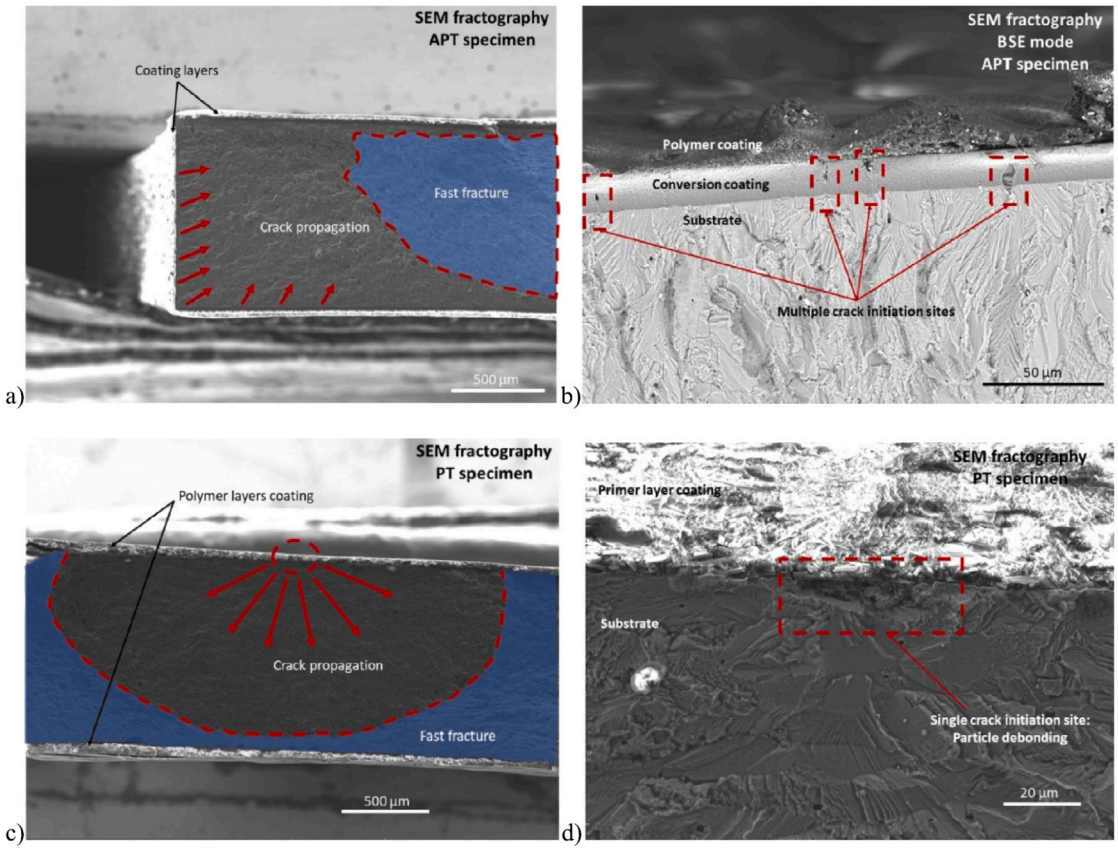

Fig. 9. SEM observations of crack initiation for an anodised and polymer coated (APT) fatigue specimen (a,b) and a polymer coated (PT) fatigue specimen (c,d) made from 7075-T6 aluminium alloy. This figure is reproduced from the paper by Vie et al. [64].

that the main crack initiation stems from the surface notches present in the as-built specimens. This observation raises the possibility that surface notches either contribute to crack initiation or support crack propagation by a mechanism similar to continuous initiation. Finally, from the examination of the fracture surfaces in the present study, which also show a large crack initiation zone (Fig. 7), the hypothesis of multiple cracking of the alpha-case at the notch roots leading to a single main crack distributed over a large crack initiation zone and followed by a continuous initiation process seems plausible.

More sophisticated analyses would be required to further elucidate these mechanisms. For example, *in situ* acoustic emission analysis during fatigue testing, similar to the method used by Vie et al. [64], could provide valuable insights. From the same perspective, fatigue testing coupled with *in situ* X-ray tomography setups using synchrotron X-ray sources should be carried out [65]. Finally, it would also be instructive to investigate the effects of SR, LF-HT and IF-HT conditions on specimens that have been machined and polished. Such an investigation could reveal whether, in the absence of critical surface defects, the microstructure or the presence of an alpha-case layer has a more significant influence on fatigue resistance.

3.5. Crack initiation site analysis

To investigate whether the presence of the alpha-case layer could promote crack initiation, the crack initiation site density was estimated in specimens under SR, LF-HT and IF-HT conditions. The idea was to study cracks that propagated during fatigue cycling, even if they did not propagate through the entire specimen section to cause failure. These are hereafter referred to as "**Secondary Fatigue Cracks**" (SFC). Fig. 10 shows an example of such a SFC, revealed after chemical etching of the longitudinal cross-section of one half of a fractured specimen tested at 450 MPa. As shown in the overall view of the specimen, a total of 6 SFC were identified and are marked with red arrows in the magnified views. SFC are oriented perpendicular to the loading direction (Mode I propagation) with a relatively small opening within the enlarged views in Fig. 10. Their initiation can often be correlated with the presence of surface notches and their propagation often extends beyond the alpha case layer.

A distinct type of crack, observed predominantly on IF-HT specimens after fracture, deserves attention. Such cracks are specifically associated with the final stage of failure, see an example marked with green arrows in Fig. 10. It is noteworthy that such cracks were only identified on the surfaces of specimens that experienced complete failure, and not on those of interrupted tests. It is therefore likely that these cracks are associated with the final stage of failure, but not with the initial stages of crack initiation or propagation. Accordingly, they are defined as "**Final Failure Cracks** (FFC)". Fig. 11 shows some of these FFC. Their relatively large opening and limited depth, correlating with the local thickness of the alpha case, are highlighted in Fig. 11.b. These features are similar to the cracks observed in the post-failure tensile specimens in Ref. [13]. In the final stages of fatigue life, the material is subjected to significantly high stresses towards the end of crack propagation, which explains the similarities between the fracture surfaces observed in the final failure region and those in the tensile specimens. Close examination reveals a dense cluster of FFC at the edge of the final failure zone, as shown schematically in Fig. 11.c. The occurrence of such FFC highlights the potential of the alpha-case layer to reduce fracture toughness, thereby accelerating final failure. This observation is in good agreement with the findings from the tensile test results [13]. From this perspective, the FFC are not the objects of primary interest to study the effect of the alpha layer on the initiation stage and overall fatigue life. Therefore, the following paragraphs will focus exclusively on the SFC.

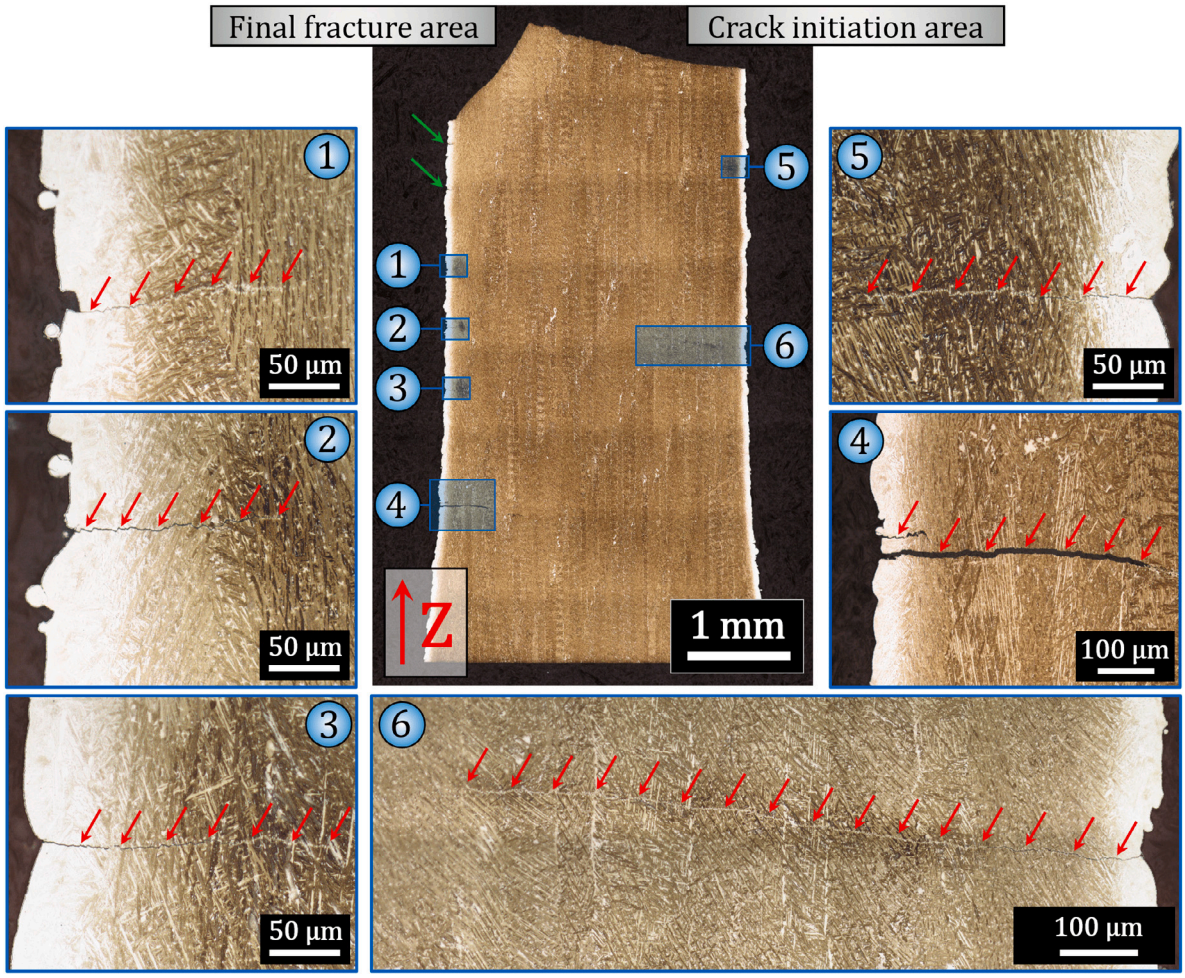

Fig. 10. Longitudinal cross-section analysis with optical microscopy of secondary fatigue cracks (SFC) in an IF-HT specimen tested at 450 MPa. The cross-section of the specimen was polished and etched with Weck's reagent. Magnified views highlight the fatigue cracks with red arrows, while green arrows near the final fracture zone indicate the location of the final fracture cracks shown in Fig. 11.

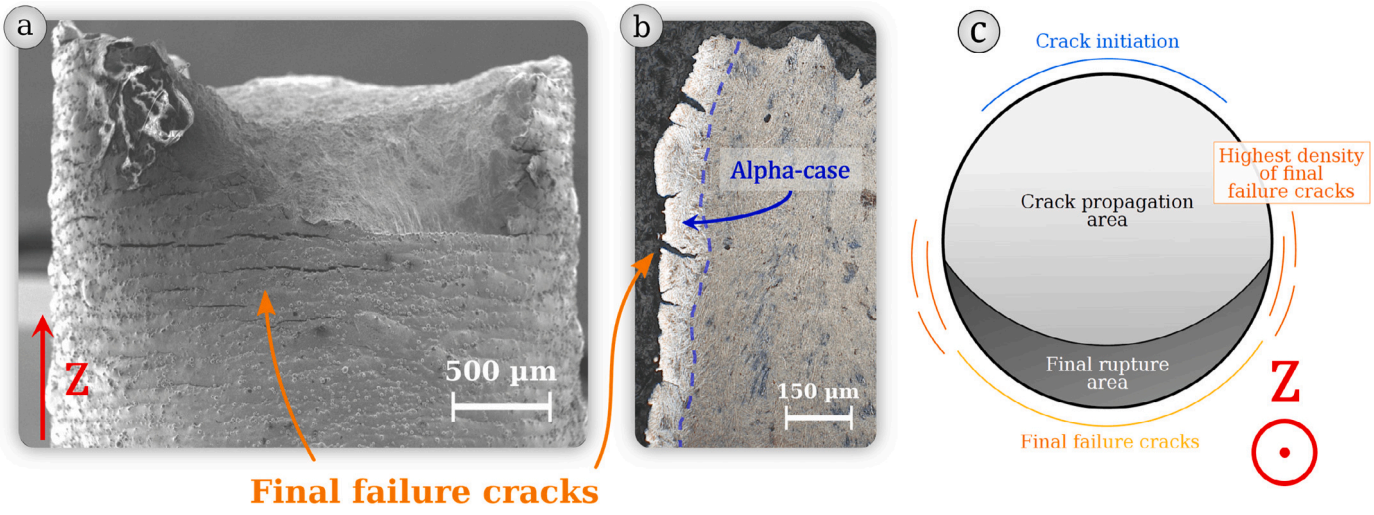

Fig. 11. Observation of final fracture cracks (FFC) in an IF-HT specimen tested at 350 MPa. SEM-SE image (a) and optical microscope image of a longitudinal cross-section after chemical etching with Weck's reagent to reveal the alpha-case in white (b). Schematic representation of an IF-HT fracture surface, showing the preferential locations of FFC (c).

From the XCT data obtained after fatigue testing, it was found that FFC with a sufficiently large opening were detectable, whereas all SFC showed a rather small opening and thus could not be detected by XCT. Therefore, in order to investigate the effect of alpha-case layers of different depths on the prevalence of SFC, a comprehensive light microscopy analysis was carried out on 11 SR, 9 LF-HT and 11 IF-HT specimens subjected to different stresses. After each test, a longitudinal cross-section of the specimen (half for fractured specimens) was

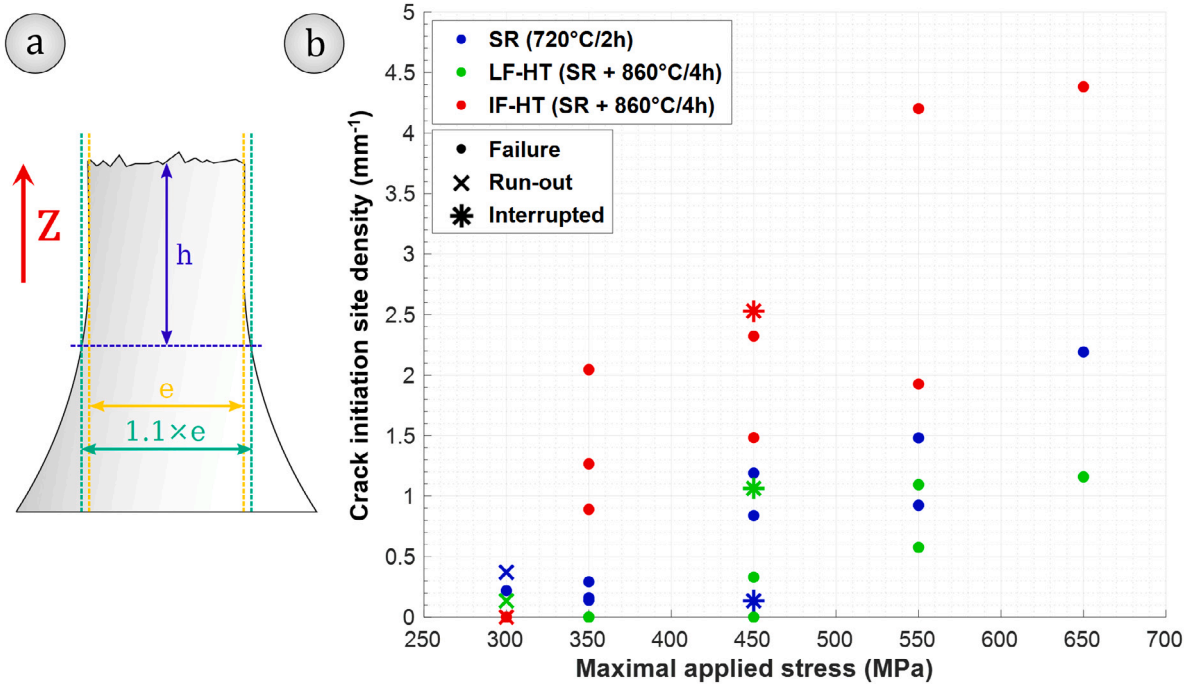

Fig. 12. Fatigue crack linear density measurements on SR, LF-HT and IF-HT specimens at different stresses. Schematic representation of the height h within which cracks are counted for each specimen (a). SFC initiation site densities measured for all specimens as a function of the maximum stress during the fatigue test (b).

prepared. This cross-section was then polished and etched with Weck's reagent. On this cross-section of thickness e near the fracture area, the SFC were identified and counted within a distance h measured between the middle of the fracture area and the beginning of the fillet radius defined as $1.1 \times e$, as illustrated in Fig. 12.a. For interrupted and run-out specimens, the h value was measured over the entire gauge length, between the beginning of the two fillet radii at $1.1 \times e$, and the thickness at the centre of the gauge area. The number of SFC counted was then normalised by h to calculate a linear SFC initiation site density in mm^{-1}. The results are presented in Fig. 12.b. The analysis shows an increase in SFC initiation density with maximum stress for all conditions, a trend consistent with the understanding that higher stresses lead to an increase in the number of nucleated cracks as reported in previous studies [62]. Closer examination of Fig. 12.b indicates that the IF-HT specimens exhibit significantly higher SFC initiation site densities at stresses greater than 300 MPa. This observation supports the hypothesis that the 70 µm thick alpha case layer in the IF-HT specimens acts as a catalyst for crack initiation during fatigue loading, potentially reducing fatigue life. This is consistent with the findings of Pilchak et al. who reported a tenfold reduction in the fatigue life of a near α Ti alloy with an alpha-case layer approximately 35 ± 5 µm thick [39]. In their work this significant reduction was attributed to both a reduced resistance to crack initiation and an accelerated crack growth rate within the oxygen-enriched region. The SFC initiation site densities for the SR and LF-HT conditions were found to be comparable, with a slight increase observed in the SR specimens. This minor difference could be attributed to the presence of a harder oxygen rich alpha-case layer close to the surface of the SR specimens, despite its relatively small thickness of 10 µm (Figs. 4 and 5).

Interestingly, previous research on the same material also reported cracking of the alpha-case under tensile loading [13]. *In situ* micro-tensile tests in the SEM were carried out on specimens after IF-HT at 860 °C/2 h, which exhibited an alpha-case layer of 48 ± 2 µm at the surface. By observing the surface of the gauge at various applied tensile stresses, it was demonstrated that cracks with a very small opening began to be visible over the entire surface of the sample at 460 MPa, i.e. still in the elastic regime (with an estimated yield stress of about 1 000 MPa). In fatigue testing at $R = 0.1$, multiple tensile loading occurs in the elastic regime, which is likely to facilitate rapid surface crack initiation in the presence of an alpha-case layer. This brittle layer should therefore be considered as a source of multiple potential fatigue initiation defects (i.e. cracks), the length of which is approximately equal to the alpha-case depth. Consequently, for the IF-HT condition of this study, the reduced fatigue life (except at 300 MPa) is likely to be explained by the presence of an alpha case layer of 70 µm.

The study of tensile properties showed that with alpha-case layers of 48 ± 2 µm (IF-HT at 860 °C/2 h), 90 ± 5 µm (IF-HT at 920 °C/2 h), and 185 ± 8 µm (IF-HT at 980 °C/2 h), the elongations to failure of the alloy decreased by an average of 25 %, 50% and 80 % respectively, compared to those obtained for the same LF-HT without alpha-case formation [13]. In terms of fatigue properties, it would therefore be expected that deeper alpha-case layers could lead to reduced fatigue life. Finally, regarding the limited effect of the alpha-case layer on the fatigue property for the SR condition, a comparison can be made with its negligible impact on ductility. Indeed, the elongations to failure measured for tensile specimens with the as-received surface condition subjected to IF-HT or LF-HT at 720 °C/2 h were similar. The limited effect on the fatigue properties, even at higher stresses, could be explained by the small depth of initiated cracks in the 10 ± 1 µm alpha case layer compared to the depth of the surface notches (see Fig. 4 and S_v values in Table 3). Therefore, if an alpha-case layer is likely to be expected after a post-processing HT carried out on L-PBF fabricated parts, applying a heat treatment at 720 °C/2 h enables the complete stress relief and partial martensite decomposition of the material [16] without leading to a severe reduction of the static and dynamic properties. Even if a higher temperature subtransus HT gives better results in terms of strength-ductility trade-off [13,42], the presence of an alpha-case layer will negatively affect both ductility and fatigue life. For example, a post-LPBF HT at 860 °C results, on average, in a 25 % reduction in elongation to failure [13] and a 50% reduction in fatigue life (see Fig. 6).

As illustrated in Fig. 6, the data at 300 MPa show significant scatter, with none of the conditions presenting clear advantages in fatigue properties over the others. Similarly, Fig. 12 shows that the SFC

initiation site densities are low at 300 MPa, regardless of the conditions tested. This observation suggests that a maximum applied fatigue stress of 300 MPa is not sufficient to significantly influence SFC propagation, even in the presence of a 70 ± 3 μm thick alpha case layer.

From the *in situ* micro-tensile tests observations of Ref. [13], it is considered that cracking occurs in the alpha-case layer during the early stages of the fatigue tests. Therefore, it is possible to calculate $K_{I,max}$ associated with these defects, which is the maximum value of the mode I (opening mode) stress intensity factor along the crack front. Since the thickness a of the alpha-case is small relative to the specimen thickness, $K_{I,max}$ can be calculated using Eq. (3) for a half penny shaped crack whose depth is equal to the alpha-case thickness a [66]:

$$K_{I,max} = 0.629 \times \sigma_{max} \times \sqrt{\pi \times \sqrt{\frac{\pi \times a^2}{2}}} \quad (3)$$

Applying Eq. (3) for the alpha-case thickness of 70 ± 3 μm under IF-HT conditions gives $K_{I,max}$ values approximately equal to 3.1 MPa $m^{1/2}$, for a maximum applied stress of 300 MPa. Interestingly, this value of the same order of magnitude as the fatigue crack growth threshold ΔK_{th} of Ti64 alloy fabricated by L-PBF, even it was not possible to measure this property within the scope of this study. For instance, Leuders et al. reported a ΔK_{th} of 3.9 ± 0.4 MPa $m^{1/2}$ at $R = 0.1$ for Ti64 fabricated by L-PBF and subjected to a post-processing heat treatment at 800 °C [67]. This suggests that at a maximum applied stress of 300 MPa, even the cracks initiated in the deepest 70 μm alpha case layer do not propagate due to the proximity of the calculated $K_{I,max}$ to the potential fatigue crack growth threshold of the material. Therefore, at 300 MPa, crack propagation only occurs for sufficiently critical surface defects (i.e. higher $K_{I,max}$), resulting in the high scatter in fatigue properties and the low density of SFC initiation sites observed.

The effect of an alpha-case layer of varying depth on near-net-shape L-PBF Ti64 specimens was investigated by various analyses: determination of fatigue properties, identification of killer defects by XCT, measurement of crack initiation site densities. The as-built surface condition, with most cracks initiated at the surface notch roots, was shown to have a predominant effect on the fatigue properties. Therefore, the microstructural changes that occur during sub-transus post-processing HT have a limited effect on fatigue resistance. However, Ti64 parts are subject to the formation of an oxygen-enriched brittle alpha-case layer below the surface if the HT protective atmosphere (vacuum, argon gas, ...) is not properly controlled. If this layer cannot be removed by post-HT surface treatments, this work suggests two possible scenarios :

- The first is that the alpha-case depth is small compared to the surface defect size (i.e. notch depth). In this study, the effect of a 10 ± 1 μm brittle layer was limited and did not exacerbate the detrimental effects of surface notches. However, such a small alpha-case layer could have a large effect on polished samples, according to Refs. [34,38,39].
- The second scenario is that the alpha case depth is large compared to the surface defect size. In this study, the 70 ± 3 μm brittle layer reduced the fatigue life of the near-net-shape samples by approximately half for applied stresses above the assumed fatigue crack growth threshold. Such a large alpha case layer could have a severe effect on polished specimens.

The lesson to be learnt from this study is to be cautious of alpha-case formation which can occur during the post-processing HT of near-net-shape Ti64 L-PBF parts. A large alpha-case layer ($\geq$ 50 μm) is detrimental to both ductility and fatigue life. However, a small alpha case layer ($\approx$ 10 μm) does not appear to be of primary concern for both tensile [13] and fatigue properties.

4. Conclusions

In this study, the fatigue properties of Ti-6Al-4V (Ti64) alloy fabricated by Laser Powder Bed Fusion (L-PBF) with as-built surfaces and subjected to three different post-processing heat treatments (HT) were investigated. The use of two annealing temperatures, Stress Relieving (SR) at 720 °C and HT at 860 °C, together with the use of IF-HT (industrial furnace) and LF-HT (laboratory furnace) conditions, allowed the generation of alpha-case layers of different thicknesses on the sample surface. It was therefore possible to investigate the effect of alpha-case layers on the surface embrittlement and fatigue properties of the material. The main results of this work are summarised below:

- The bulk microstructures of all samples after HT consist of a mixture of $\alpha + \beta$ phases in a chessboard pattern of prior β-grain structures observable in planes perpendicular to the building direction. The size of α laths and the fraction of β phase are larger in the IF-HT and LF-HT conditions (approximately 1 μm and 4%) compared to the SR condition (approximately 0.6 μm and 2 %).
- The SR and IF-HT conditions show a distinct alpha-case layer at the surface, with thicknesses estimated to be 10 ± 1 μm and 70 ± 3 μm respectively. These layers result from oxygen diffusion from the surface, leading to oxygen concentration profiles associated with increased surface hardness. In contrast, the LF-HT condition shows no discernible alpha-case layer and only a moderate increase in surface hardness.
- The fatigue properties are consistent with those reported in the literature for L-PBF Ti64 specimens with as-built surfaces. The fatigue strength at 10^7 cycles was estimated to be around 250 MPa. Among the conditions studied, only the IF-HT condition, which has the thickest alpha-case layer, exhibited a decrease in fatigue resistance, while the SR and LF-HT conditions demonstrated similar properties.
- Under all conditions, fatigue crack initiation occurred systematically at the surface of the specimens. 3D surface characterisation using X-ray Computed Tomography (XCT) before and after fatigue testing revealed that, in most cases, cracks initiated at surface notches. This finding emphasises the primary influence of as-built surface conditions over microstructure for Ti64 components fabricated by L-PBF.
- Post-mortem examination of the specimens allowed identification and counting of secondary fatigue cracks (SFC) distributed along the height of the specimen and extending beyond the alpha-case layer. The linear densities of SFC initiation sites in specimens from the IF-HT condition were significantly higher than those in the other two conditions for applied stresses above 300 MPa. This emphasises the role of the 70 ± 3 μm deep alpha case layer in promoting crack initiation and thus reducing fatigue life.

This work shows that end-users should consider more carefully the possibility of forming an alpha-case layer during post processing HT, as this can reduce the fatigue life of the material.

CRediT authorship contribution statement

Quentin Gaillard: Writing – original draft, Visualization, Investigation, Conceptualization. **Florian Steinhilber:** Writing – original draft, Visualization, Investigation, Conceptualization. **Amélie Larguier:** Investigation. **Xavier Boulnat:** Writing – review & editing, Validation, Supervision, Conceptualization. **Jean-Yves Buffiere:** Writing – review & editing, Validation, Supervision, Funding acquisition, Conceptualization. **Guilhem Martin:** Writing – review & editing, Supervision. **Sylvain Dancette:** Writing – review & editing, Supervision. **Sophie Cazottes:** Writing – review & editing, Supervision. **Rémy Dendievel:** Validation, Supervision, Funding acquisition. **Christophe Desrayaud:** Validation, Supervision, Funding acquisition.

Declaration of competing interest

The authors declare that they have no known competing financial interests or personal relationships that could have appeared to influence the work reported in this paper.

Data availability

Data will be made available on request.

Acknowledgements

This work, conducted at LGF, MATEIS and SiMaP laboratories, falls within the framework of the AEROPRINT project, which received support from the Auvergne-Rhône-Alpes Region, France and the company Dassault Aviation, France. The authors are grateful for their financial support and extend special thanks to the project team at the Argonay production site for fabricating the samples used in this study.

References

[1] Vafadar A, Guzzomi F, Rassau A, Hayward K. Advances in metal additive manufacturing: a review of common processes, industrial applications, and current challenges. Appl Sci 2021;11(3):1213. http://dx.doi.org/10.3390/app11031213.
[2] DebRoy T, Wei H, Zuback J, Mukherjee T, Elmer J, Milewski J, et al. Additive manufacturing of metallic components – Process, structure and properties. Prog Mater Sci 2018;92:112–224. http://dx.doi.org/10.1016/j.pmatsci.2017.10.001.
[3] Najmon JC, Raeisi S, Tovar A. Review of additive manufacturing technologies and applications in the aerospace industry. In: Additive manufacturing for the aerospace industry. Elsevier; 2019, p. 7–31. http://dx.doi.org/10.1016/B978-0-12-814062-8.00002-9.
[4] Liu S, Shin YC. Additive manufacturing of Ti6Al4V alloy: A review. Mater Des 2019;164:107552. http://dx.doi.org/10.1016/j.matdes.2018.107552.
[5] Agius D, Kourousis K, Wallbrink C. A review of the as-built SLM Ti-6Al-4V mechanical properties towards achieving fatigue resistant designs. Metals 2018;8(1):75. http://dx.doi.org/10.3390/met8010075.
[6] Ahmad B, van der Veen SO, Fitzpatrick ME, Guo H. Residual stress evaluation in selective-laser-melting additively manufactured titanium (Ti-6Al-4V) and inconel 718 using the contour method and numerical simulation. Addit Manuf 2018;22:571–82. http://dx.doi.org/10.1016/j.addma.2018.06.002.
[7] Yang J, Yu H, Yin J, Gao M, Wang Z, Zeng X. Formation and control of martensite in Ti-6Al-4V alloy produced by selective laser melting. Mater Des 2016;108:308–18. http://dx.doi.org/10.1016/j.matdes.2016.06.117.
[8] He Y, Ma Y, Zhang W, Wang Z. Anisotropic tensile and fatigue properties of laser powder bed fusion Ti6Al4V under high temperature. Eng Fract Mech 2022;276:108948. http://dx.doi.org/10.1016/j.engfracmech.2022.108948.
[9] Kasperovich G, Haubrich J, Gussone J, Requena G. Correlation between porosity and processing parameters in TiAl6V4 produced by selective laser melting. Mater Des 2016;105:160–70. http://dx.doi.org/10.1016/j.matdes.2016.05.070.
[10] Cao F, Zhang T, Ryder MA, Lados DA. A review of the fatigue properties of additively manufactured Ti-6Al-4V. JOM 2018;70(3):349–57. http://dx.doi.org/10.1007/s11837-017-2728-5.
[11] Cabanettes F, Joubert A, Chardon G, Dumas V, Rech J, Grosjean C, et al. Topography of as built surfaces generated in metal additive manufacturing: A multi scale analysis from form to roughness. Precis Eng 2018;52:249–65. http://dx.doi.org/10.1016/j.precisioneng.2018.01.002.
[12] Vrancken B, Thijs L, Kruth J-P, Van Humbeeck J. Heat treatment of Ti6Al4V produced by selective laser melting: microstructure and mechanical properties. J Alloys Compd 2012;541:177–85. http://dx.doi.org/10.1016/j.jallcom.2012.07.022.
[13] Gaillard Q, Boulnat X, Cazottes S, Dancette S, Desrayaud C. Strength/ductility trade-off of Laser Powder Bed Fusion Ti-6Al-4V: Synergetic effect of alpha-case formation and microstructure evolution upon heat treatments. Addit Manuf 2023;76:103772. http://dx.doi.org/10.1016/j.addma.2023.103772.
[14] Cain V, Thijs L, Van Humbeeck J, Van Hooreweder B, Knutsen R. Crack propagation and fracture toughness of Ti6Al4V alloy produced by selective laser melting. Addit Manuf 2015;5:68–76. http://dx.doi.org/10.1016/j.addma.2014.12.006.
[15] Kumar P, Ramamurty U. Microstructural optimization through heat treatment for enhancing the fracture toughness and fatigue crack growth resistance of selective laser melted Ti 6Al 4V alloy. Acta Mater 2019;169:45–59. http://dx.doi.org/10.1016/j.actamat.2019.03.003.
[16] Gaillard Q, Cazottes S, Boulnat X, Dancette S, Desrayaud C. Microstructure, texture and mechanical properties with raw surface states of Ti-6Al-4V parts built by L-PBF. Proc CIRP 2022;108:698–703. http://dx.doi.org/10.1016/j.procir.2022.03.108.
[17] Ter Haar GM, Becker TH. Low temperature stress relief and martensitic decomposition in selective laser melting produced Ti6Al4V. Mater Des Process Commun 2021;3(1). http://dx.doi.org/10.1002/mdp2.138.
[18] Funch CV, Palmas A, Somlo K, Valente EH, Cheng X, Poulios K, et al. Targeted heat treatment of additively manufactured Ti-6Al-4V for controlled formation of Bi-lamellar microstructures. J Mater Sci Technol 2021;81:67–76. http://dx.doi.org/10.1016/j.jmst.2021.01.004.
[19] Thöne M, Leuders S, Riemer A, Tröster T, Richard H. Influence of heat-treatment of selective laser melting products - e.g. Ti6Al4V. In: 2012 international solid freeform fabrication symposium. University of Texas at Austin; 2012, http://dx.doi.org/10.26153/TSW/15368.
[20] Tao P, Li H-x, Huang B-y, Hu Q-d, Gong S-l, Xu Q-y. Tensile behavior of Ti-6Al-4V alloy fabricated by selective laser melting: Effects of microstructures and as-built surface quality. China Foundry 2018;15(4):243–52. http://dx.doi.org/10.1007/s41230-018-8064-8.
[21] Meier B, Godja N, Warchomicka F, Belei C, Schäfer S, Schindel A, et al. Influences of surface, heat treatment, and print orientation on the anisotropy of the mechanical properties and the impact strength of Ti 6Al 4V processed by laser powder bed fusion. J Manuf Mater Process 2022;6(4):87. http://dx.doi.org/10.3390/jmmp6040087.
[22] Bagehorn S, Wehr J, Maier H. Application of mechanical surface finishing processes for roughness reduction and fatigue improvement of additively manufactured Ti-6Al-4V parts. Int J Fatigue 2017;102:135–42. http://dx.doi.org/10.1016/j.ijfatigue.2017.05.008.
[23] Kasperovich G, Hausmann J. Improvement of fatigue resistance and ductility of TiAl6V4 processed by selective laser melting. J Mater Process Technol 2015;220:202–14. http://dx.doi.org/10.1016/j.jmatprotec.2015.01.025.
[24] Chastand V, Quaegebeur P, Maia W, Charkaluk E. Comparative study of fatigue properties of Ti-6Al-4V specimens built by electron beam melting (EBM) and selective laser melting (SLM). Mater Charact 2018;143:76–81. http://dx.doi.org/10.1016/j.matchar.2018.03.028.
[25] Carrion PE, Soltani-Tehrani A, Phan N, Shamsaei N. Powder recycling effects on the tensile and fatigue behavior of additively manufactured Ti-6Al-4V parts. JOM 2019;71(3):963–73. http://dx.doi.org/10.1007/s11837-018-3248-7.
[26] Yu H, Li F, Wang Z, Zeng X. Fatigue performances of selective laser melted Ti-6Al-4V alloy: Influence of surface finishing, hot isostatic pressing and heat treatments. Int J Fatigue 2019;120:175–83. http://dx.doi.org/10.1016/j.ijfatigue.2018.11.019.
[27] Kahlin M, Ansell H, Moverare J. Fatigue behaviour of notched additive manufactured Ti6Al4V with as-built surfaces. Int J Fatigue 2017;101:51–60. http://dx.doi.org/10.1016/j.ijfatigue.2017.04.009.
[28] Masuo H, Tanaka Y, Morokoshi S, Yagura H, Uchida T, Yamamoto Y, et al. Influence of defects, surface roughness and HIP on the fatigue strength of Ti-6Al-4V manufactured by additive manufacturing. Int J Fatigue 2018;117:163–79. http://dx.doi.org/10.1016/j.ijfatigue.2018.07.020.
[29] Persenot T, Burr A, Martin G, Buffiere J-Y, Dendievel R, Maire E. Effect of build orientation on the fatigue properties of as-built Electron Beam Melted Ti-6Al-4V alloy. Int J Fatigue 2019;118:65–76. http://dx.doi.org/10.1016/j.ijfatigue.2018.08.006.
[30] Greitemeier D, Dalle Donne C, Syassen F, Eufinger J, Melz T. Effect of surface roughness on fatigue performance of additive manufactured Ti–6Al–4V. Mater Sci Technol 2016;32(7):629–34. http://dx.doi.org/10.1179/1743284715Y.0000000053.
[31] Wycisk E, Emmelmann C, Siddique S, Walther F. High cycle fatigue (HCF) performance of Ti-6Al-4V alloy processed by selective laser melting. Adv Mater Res 2013;816–817:134–9. http://dx.doi.org/10.4028/www.scientific.net/AMR.816-817.134.
[32] Pyka G, Kerckhofs G, Papantoniou I, Speirs M, Schrooten J, Wevers M. Surface roughness and morphology customization of additive manufactured open porous Ti6Al4V structures. Materials 2013;6(10):4737–57. http://dx.doi.org/10.3390/ma6104737.
[33] Zhang J, Chaudhari A, Wang H. Surface quality and material removal in magnetic abrasive finishing of selective laser melted 316L stainless steel. J Manuf Process 2019;45:710–9. http://dx.doi.org/10.1016/j.jmapro.2019.07.044.
[34] Gaddam R, Antti M-L, Pederson R. Influence of alpha-case layer on the low cycle fatigue properties of Ti-6Al-2Sn-4Zr-2Mo alloy. Mater Sci Eng A 2014;599:51–6. http://dx.doi.org/10.1016/j.msea.2014.01.059.
[35] Casadebaigt A, Hugues J, Monceau D. High temperature oxidation and embrittlement at 500–600 °C of Ti-6Al-4V alloy fabricated by laser and electron beam melting. Corros Sci 2020;175:108875. http://dx.doi.org/10.1016/j.corsci.2020.108875.
[36] Dong E, Yu W, Cai Q. Alpha-case kinetics and high temperature plasticity of Ti-6Al-4V alloy oxidized in Different Phase Regions. Procedia Eng 2017;207:2149–54. http://dx.doi.org/10.1016/j.proeng.2017.10.973.
[37] Seth P, Jha JS, Alankar A, Mishra SK. Alpha-case formation in Ti–6Al–4V in a different oxidizing environment and its effect on tensile and fatigue crack growth behavior. Oxid Met 2022;97(1–2):77–95. http://dx.doi.org/10.1007/s11085-021-10079-y.
[38] Fukai H, Iizumi H, Minakawa K-n, Ouchi C. The effects of the oxygen-enriched surface layer on mechanical properties of $A+\beta$ type titanium alloys. ISIJ Int 2005;45(1):133–41. http://dx.doi.org/10.2355/isijinternational.45.133.

[39] Pilchak AL, Porter WJ, John R. Room temperature fracture processes of a near-α titanium alloy following elevated temperature exposure. J Mater Sci 2012;47(20):7235–53. http://dx.doi.org/10.1007/s10853-012-6673-y.
[40] Findlay S, Harrison N. Why aircraft fail. Mater Today 2002;5(11):18–25. http://dx.doi.org/10.1016/S1369-7021(02)01138-0.
[41] Kahlin M, Ansell H, Basu D, Kerwin A, Newton L, Smith B, et al. Improved fatigue strength of additively manufactured Ti6Al4V by surface post processing. Int J Fatigue 2020;134:105497. http://dx.doi.org/10.1016/j.ijfatigue.2020.105497.
[42] Zhang X-Y, Fang G, Leeflang S, Böttger AJ, A. Zadpoor A, Zhou J. Effect of subtransus heat treatment on the microstructure and mechanical properties of additively manufactured Ti-6Al-4V alloy. J Alloys Compd 2018;735:1562–75. http://dx.doi.org/10.1016/j.jallcom.2017.11.263.
[43] Steinhilber F, Lachambre J, Coeurjolly D, Buffiere J-Y, Martin G, Dendievel R. A methodology for the 3D characterization of surfaces using X-ray computed tomography: Application to additively manufactured parts. Addit Manuf 2024;84:104144. http://dx.doi.org/10.1016/j.addma.2024.104144.
[44] Steinhilber F. on the use of X-ray computed tomography to investigate the influence of surface integrity on the fatigue properties of additively manufactured ti64 (Ph.D. thesis), Université de Lyon, Lyon; 2024.
[45] Gaillard Q, Boulnat X, Cazottes S, Dancette S, Desrayaud C. On the transformation temperatures of Ti-6Al-4V: Effect of oxygen pick-up during Laser Powder Bed Fusion. Mater Charact 2023;205:113323. http://dx.doi.org/10.1016/j.matchar.2023.113323.
[46] Lakroune Y, Connétable D, Hugues J, Hermantier P, Barriobero-Vila P, Dehmas M. Microstructural evolution during post heat treatment of the Ti–6Al–4V alloy manufactured by laser powder bed fusion. J Mater Res Technol 2023;23:1980–94. http://dx.doi.org/10.1016/j.jmrt.2023.01.123.
[47] Kumar P, Prakash O, Ramamurty U. Micro-and meso-structures and their influence on mechanical properties of selectively laser melted Ti-6Al-4V. Acta Mater 2018;154:246–60. http://dx.doi.org/10.1016/j.actamat.2018.05.044.
[48] Neikter M, Huang A, Wu X. Microstructural characterization of binary microstructure pattern in selective laser-melted Ti-6Al-4V. Int J Adv Manuf Technol 2019;104(1–4):1381–91. http://dx.doi.org/10.1007/s00170-019-04002-8.
[49] Haghdadi N, DeMott R, Stephenson P, Liao X, Ringer S, Primig S. Five-parameter characterization of intervariant boundaries in additively manufactured Ti-6Al-4V. Mater Des 2020;196:109177. http://dx.doi.org/10.1016/j.matdes.2020.109177.
[50] Simonelli M, Tse YY, Tuck C. On the texture formation of selective laser melted Ti-6Al-4V. Metall Mater Trans A 2014;45(6):2863–72. http://dx.doi.org/10.1007/s11661-014-2218-0.
[51] Facchini L, Magalini E, Robotti P, Molinari A, Höges S, Wissenbach K. Ductility of a Ti-6Al-4V alloy produced by selective laser melting of prealloyed powders. Rapid Prototyp J 2010;16(6):450–9. http://dx.doi.org/10.1108/13552541011083371.
[52] Gaddam R, Sefer B, Pederson R, Antti M-L. Study of alpha-case depth in Ti-6Al-2Sn-4Zr-2Mo and Ti-6Al-4V. IOP Conf Ser: Mater Sci Eng 2013;48:012002. http://dx.doi.org/10.1088/1757-899X/48/1/012002.
[53] Vaché N, Monceau D. Oxygen diffusion modeling in titanium alloys: new elements on the analysis of microhardness profiles. Oxid Met 2020;93(1–2):215–27. http://dx.doi.org/10.1007/s11085-020-09956-9.
[54] Vaché N, Cadoret Y, Dod B, Monceau D. Modeling the oxidation kinetics of titanium alloys: Review, method and application to Ti-64 and Ti-6242s alloys. Corros Sci 2021;178:109041. http://dx.doi.org/10.1016/j.corsci.2020.109041.
[55] Ciszak C, Monceau D, Desgranges C. Modelling the high temperature oxidation of titanium alloys: Development of a new numerical tool PyTiOx. Corros Sci 2020;176:109005. http://dx.doi.org/10.1016/j.corsci.2020.109005.
[56] Liu Z, Welsch G. Literature survey on diffusivities of oxygen, aluminum, and vanadium in alpha titanium, beta titanium, and in rutile. Metall Trans A 1988;19(4):1121–5. http://dx.doi.org/10.1007/BF02628396.
[57] Kahveci A, Welsch G. Effect of oxygen on the hardness and alpha/beta phase ratio of Ti6Al4V alloy. Scr Metall 1986;20(9):1287–90. http://dx.doi.org/10.1016/0036-9748(86)90050-5.
[58] Yan M, Xu W, Dargusch MS, Tang HP, Brandt M, Qian M. Review of effect of oxygen on room temperature ductility of titanium and titanium alloys. Powder Metall 2014;57(4):251–7. http://dx.doi.org/10.1179/1743290114Y.0000000108.
[59] Vayssette B, Saintier N, Brugger C, Elmay M, Pessard E. Surface roughness of Ti-6Al-4V parts obtained by SLM and EBM: Effect on the High Cycle Fatigue life. Procedia Eng 2018;213:89–97. http://dx.doi.org/10.1016/j.proeng.2018.02.010.
[60] Greitemeier D, Palm F, Syassen F, Melz T. Fatigue performance of additive manufactured TiAl6V4 using electron and laser beam melting. Int J Fatigue 2017;94:211–7. http://dx.doi.org/10.1016/j.ijfatigue.2016.05.001.
[61] Le V-D, Pessard E, Morel F, Prigent S. Fatigue behaviour of additively manufactured Ti-6Al-4V alloy: The role of defects on scatter and statistical size effect. Int J Fatigue 2020;140:105811. http://dx.doi.org/10.1016/j.ijfatigue.2020.105811.
[62] Schijve J, editor. Fatigue of structures and materials. Dordrecht: Springer Netherlands; 2009, http://dx.doi.org/10.1007/978-1-4020-6808-9.
[63] Ogden H, Jaffee R. The effects of carbon, oxygen, and nitrogen on the mechanical properties of titanium and titanium alloys. Tech. rep. TML-20, 4370612, 1955, http://dx.doi.org/10.2172/4370612.
[64] Vié T, Deschanel S, Godin N, Normand B. On the effect of coatings on the tensile and fatigue properties of 7075-T6 aluminum alloy monitored with acoustic Emission (AE): Towards lifetime estimation. Int J Fatigue 2023;171:107578. http://dx.doi.org/10.1016/j.ijfatigue.2023.107578.
[65] Buffiere J-Y, Maire E, Adrien J, Masse J-P, Boller E. In situ experiments with X ray tomography: An attractive tool for experimental mechanics. Exp Mech 2010;50(3):289–305. http://dx.doi.org/10.1007/s11340-010-9333-7.
[66] Nadot Y. Fatigue from defect: Influence of size, type, position, morphology and loading. Int J Fatigue 2022;154:106531. http://dx.doi.org/10.1016/j.ijfatigue.2021.106531.
[67] Leuders S, Thöne M, Riemer A, Niendorf T, Tröster T, Richard H, et al. On the mechanical behaviour of titanium alloy TiAl6V4 manufactured by selective laser melting: Fatigue resistance and crack growth performance. Int J Fatigue 2013;48:300–7. http://dx.doi.org/10.1016/j.ijfatigue.2012.11.011.